Optimized Vivid-derived Magnets photodimerizers for subcellular optogenetics in mammalian cells

Lorena Benedetti[1,2,$], Jonathan S. Marvin[3], Hanieh Falahati[1,2], Andres Guillén-Samander[1,2],

Loren L. Looger[3*] and Pietro De Camilli[1,2,4,5*]

Affiliations:

[1]Department of Neuroscience and Cell Biology, Yale University School of Medicine, New Haven, CT 06510, USA.

[2]Howard Hughes Medical Institute, Yale University School of Medicine, New Haven, CT 06510, USA.

[3]Howard Hughes Medical Institute, Janelia Research Campus, Ashburn, VA 20147, USA.

[4]Kavli Institute for Neuroscience, Yale University School of Medicine, New Haven, CT 06510, USA.

[5]Program in Cellular Neuroscience, Neurodegeneration and Repair, Yale University School of Medicine, New Haven, CT 06510 USA.

[$]current address: benedettil@janelia.hhmi.org

*Address correspondence to:

Pietro De Camilli: pietro.decamilli@yale.edu

Loren L. Looger: loogerl@janelia.hhmi.org

ABSTRACT

Light-inducible dimerization protein modules enable precise temporal and spatial control of biological processes in non-invasive fashion. Among them, Magnets are small modules engineered from the *Neurospora crassa* photoreceptor Vivid by orthogonalizing the homodimerization interface into complementary heterodimers. Both Magnets components, which are well-tolerated as protein fusion partners, are photoreceptors requiring simultaneous photoactivation to interact, enabling high spatiotemporal confinement of dimerization with a single-excitation wavelength. However, Magnets require concatemerization for efficient responses and cell preincubation at 28^{o}C to be functional. Here we overcome these limitations by engineering an optimized Magnets pair requiring neither concatemerization nor low temperature preincubation. We validated these "enhanced" Magnets (eMags) by using them to rapidly and reversibly recruit proteins to subcellular organelles, to induce organelle contacts, and to reconstitute OSBP-VAP ER-Golgi tethering implicated in phosphatidylinositol-4-phosphate transport and metabolism. eMags represent a very effective tool to optogenetically manipulate physiological processes over whole cells or in small subcellular volumes.

Keywords: LOV domain, Light-dependent dimerizers, organelle contacts, VAP, Vivid, OSBP, PI4P, PI(4,5)P_2, contact sites, OCRL

INTRODUCTION

Macromolecular interactions between and amongst proteins and organelles mediate a considerable amount of biochemical signaling processes. A principal method of testing the physiological significance of such interactions is to drive their association with a user-supplied stimulus such as light or drugs. Typically, two different components, each fused to a specific protein, come together ("heterodimerize") to reconstitute a given protein-protein interaction following addition of a small molecule (DeRose et al., 2013; Putyrski and Schultz, 2012; Spencer et al., 1993) or upon light illumination (Losi et al., 2018; Rost et al., 2017). Light offers much greater spatial and temporal resolution than drugs, and as such, optogenetic dimerizers are generally used to probe phenomena at cellular and subcellular scales. At the organism scale, light is much less invasive but suffers from penetration issues.

Photodimerizers have been successfully used to manipulate a variety of cellular processes, including signaling networks (Gasser et al., 2014; Grusch et al., 2014; Guglielmi et al., 2015; Idevall-Hagren et al., 2012; Toettcher et al., 2013, 2011; Wu et al., 2009) organelle trafficking (Bergeijk et al., 2015; Duan et al., 2015), nuclear import/export (Lerner et al., 2018; Niopek et al., 2016, 2014), cytoskeletal dynamics (Haren et al., 2018), and phase separation (Bracha et al., 2018; Dine et al., 2018; Shin et al., 2017), among others.

Both natural and synthetic photoswitches (Guntas et al., 2014; Losi et al., 2018; Lungu et al., 2012; Rost et al., 2017; Strickland et al., 2012) have been used for these studies, each with its own advantages and drawbacks. Limitations of existing systems include necessity of adding exogenous cofactors (Levskaya et al., 2009), large size adversely affecting function of targeted proteins (Kaberniuk et al., 2016; Kennedy et al., 2010; Levskaya et al., 2009; Yazawa et al., 2009), non-trivial levels of basal dimerization in the dark (Guntas et al., 2014; Hallett et al., 2015; Nijenhuis et al., 2020; Zimmerman et al., 2016), poor light-dependent dimerization efficiency (Kawano et al., 2015; Strickland et al., 2012), and improper homo-, instead of heterodimerization (Bugaj et al., 2013; Che et al., 2015; Duan et al., 2017; Taslimi et al., 2016).

One popular photodimerizer pair is "Magnets", engineered from the *Neurospora crassa* Vivid photoreceptor, which comprises an N-terminal Ncap domain responsible for homodimerization and a C-terminal light-oxygen-voltage-sensing (LOV) domain (Kawano et al., 2015). Magnets employ the

ubiquitous cofactor flavin adenine dinucleotide (FAD) as the light-sensing moiety. The Magnets pair was engineered from the Vivid homodimer by introducing complementary charges, giving rise to nMag (negative Magnet) and pMag (positive Magnet). The two Magnets components are quite small (150 aa) for photodimerizers, exhibit relatively fast association and dissociation kinetics, and function when fused to a broad range of proteins, including peripheral and intrinsic membrane proteins (Benedetti et al., 2018; Kawano et al., 2016, 2015). Furthermore, heterodimerization of Magnets requires light-dependent activation of both components, rather than just one. This property results in low levels of background activity and allows induction of dimer formation with single-wavelength excitation in small cytoplasmic volumes (Benedetti et al., 2018).

However, the Magnets system has two prominent shortcomings. First, the low thermodynamic stability of the Magnets components precludes their proper expression and folding at 37^{o}C. Thus, they cannot be used in mammals. When used in cultured mammalian cells they require a preincubation at low temperature (28^{o}C) for 12 hours to allow expression and folding. Second, as the Magnets components heterodimerize with low efficiency, robust activation requires concatemerization (Furuya et al., 2017; Kawano et al., 2015), which may affect trafficking, motility and function of target proteins, create vector payload constraints, and give rise to recombination and/or silencing of the sequence repeats.

Here, we overcome these limitations of the Magnets by structure-guided protein engineering and validation by cellular assays. The resulting reagents, “enhanced Magnets” (eMags), have greater thermal stability and dimerization efficiency, as well as faster association and dissociation kinetics. We confirmed their effectiveness in a variety of applications including protein recruitment to different organelles, the generation/expansion of organelle contact sites, and the rapid and reversible reconstitution of VAP-dependent inter-organelle tethers that have key regulatory functions in lipid transport.

RESULTS

Optimization of the Magnets heterodimer interface

Optimal photo-heterodimerizer performance convolves together several parameters: i) Efficient, fast interaction of the two different components upon light stimulus, ii) little or no formation of homodimers – which would compete with productive heterodimer complexes, iii) low background before light stimulus; and ideally, iv) fast heterodimer dissociation following light offset. The existing Magnets systems, especially the Fast1 and Fast2 variants with fast dissociation kinetics (Kawano et al., 2015), have weak dimerization efficiency and thus perform poorly on the first criterion, necessitating the use of concatemers (usually 3 copies) of either or both monomers to achieve acceptable reconstitution in a number of settings (Benedetti et al., 2018; Furuya et al., 2017; Kawano et al., 2015). A pair with greater dimerization efficiency would be desirable, ideally allowing single copies of the complementary Magnets to suffice. With the goal of engineering such a pair, we first established a robust screen for reconstitution of Magnets dimerization using light-dependent accumulation of a protein at the outer mitochondrial membrane (Benedetti et al., 2018) (**Figure 1A**), which is readily visible and quantifiable. The nMagHigh1 monomer, tagged with the green fluorescent protein EGFP, was used as bait on the outer mitochondrial membrane by fusion to the transmembrane C-terminal helix from OMP25 ("nMag-EGFP-Mito") (**Figure 1-figure supplement 1A** and **Supplementary File 1)**. The pMagFast2 monomer, tagged with the red fluorescent protein TagRFP-T (Shaner et al., 2008), was used as the cytoplasmic prey ("pMag-TagRFP-T"; **Figure 1-figure supplement 1A** , **Supplementary File 2**). We co-expressed both constructs in HeLa cells by co-transfection, grew cells at 28°C for 24 hours, and tested light-dependent prey capture and release by the bait (**Figure 1B, Video 1**). Short (1 min of 200-ms light pulses every 2 s) irradiation with cyan light (488 nm; $3x10^{-3}$ W/cm^2) sufficed to recruit the prey from its diffuse cytoplasmic distribution (**Figure 1B**, 2nd panel) to mitochondria (**Figure 1B**, 3rd panel), resulting in a precise overlapping localization of prey and bait (**Figure 1-figure supplement 2A**). This recruitment was reversible following light offset (**Figure 1B**, 4th panel). Importantly, excitation light for TagRFP-T, as well as that for mCherry and the infrared fluorescent protein iRFP (Shcherbakova and Verkhusha, 2013), is well outside the action spectrum of LOV domain proteins (400-500 nm light excitation) (Losi et al., 2018); EGFP excitation light is coincident with Magnets activation and is thus used sparingly in these experiments.

Figure 1

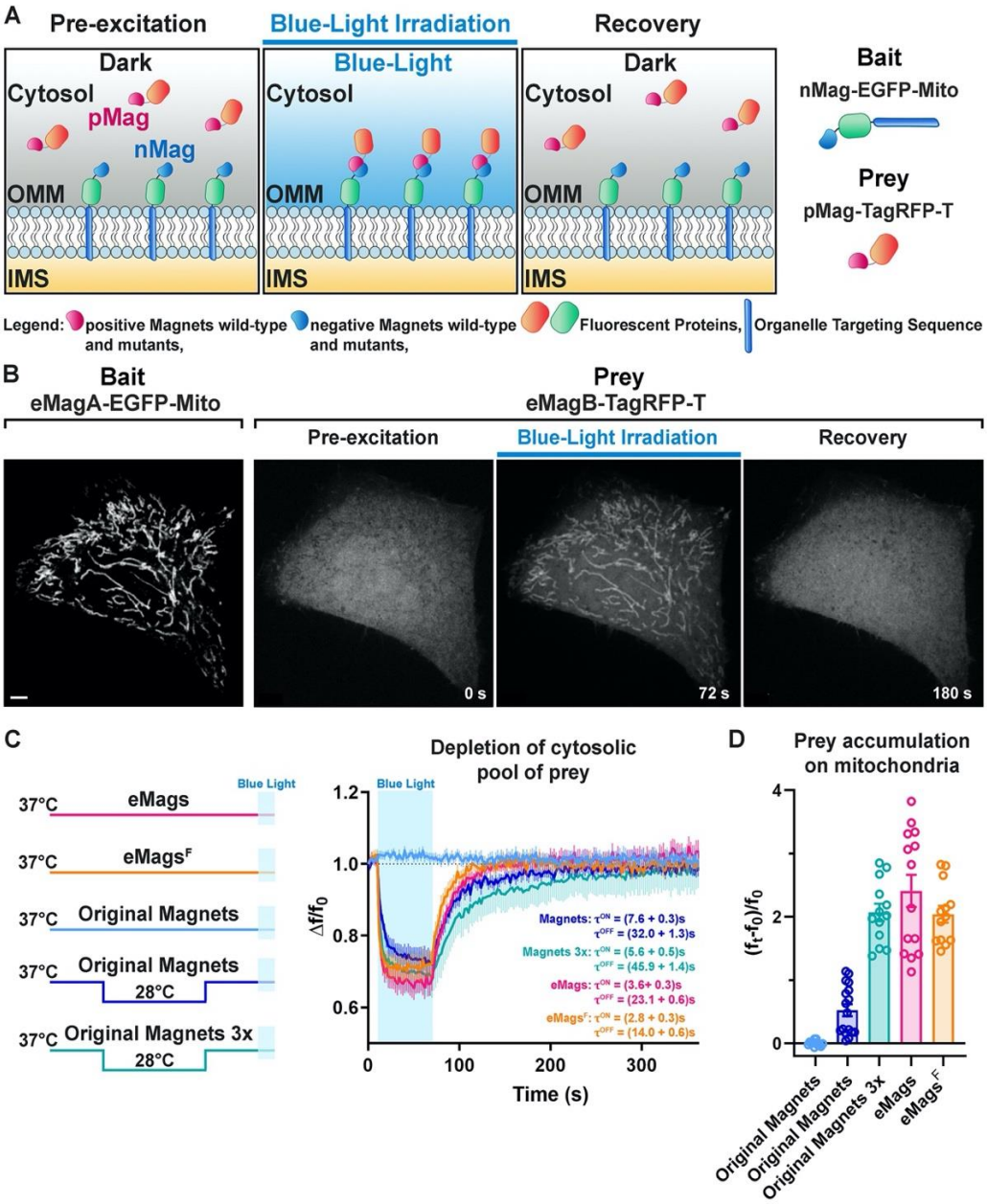

Figure 1: Development and validation of enhanced Magnets (eMags).

A. Schematic of the assay used to screen for light-dependent Magnets heterodimerization in living cells. The negative Magnet was anchored to the outer mitochondrial membrane (OMM), while the positive Magnet was cytosolic and recruited to mitochondria upon heterodimerization. IMS = Intermembrane space.

B. Representative example of reversible light-dependent recruitment of eMagB-TagRFP-T (prey, enhanced pMag) to mitochondria in HeLa cells expressing the mitochondrial Mito-EGFP-eMagA (bait, enhanced nMag). Confocal images. Scale bar: 10 μm.

C. Left: schematic of experiment, with original Magnets being incubated at either 28°C or 37°C before assay. Right: prey depletion from the cytosol (due to its recruitment to mitochondria) for each regime (original Magnets (37°C): n = 13 cells, original Magnets (28°C): 17 cells, original Magnets 3x (28°C): 13 cells, eMags: 14 cells, eMags^F: 13 cells; from 3 independent experiments).

D. Amount of prey recruited to mitochondria after 60 s of blue light exposure.

Next, we began the process of Magnets redesign by optimizing the placement of charge-complementing amino acids in the Vivid dimer interface, using the crystal structure of the light-activated dimer (PDB ID 3RH8) (Vaidya et al., 2011) (**Figure 1-figure supplement 3A-C**) as a guide, and mitochondrial recruitment as the testbed. The original Magnets pair was built upon the mutations Ile52 and Met55 to Arg (positive Magnet) and Ile52 to Asp and Met55 to Gly (negative Magnet) within the Ncap domain (See **Figure 1-figure supplement 3A**), which mediates dimerization. To achieve more efficient dimerization, we first sought to optimize charge placement at the interface. Substitution of Asp52 to Glu in nMag-Asp52Glu to modify the position of the negative charges somewhat disrupted heterodimerization, consistent with Kawano et al., 2015 (Kawano et al., 2015). We next tried to introduce two negative charges into nMag, at the same two sites where positive charges had been introduced into pMag. nMag-Gly55Glu completely inhibited heterodimerization, whereas nMag-Gly55Asp somewhat improved it (**Figure 1-figure supplement 3D**). Adding a third positive charge to pMag at position 48 also completely disrupted heterodimerization. In the end, we left the charges alone and instead sought to improve heterodimer interface packing and helical preference with nMag-Gly55Ala, which indeed improved both heterodimerization efficiency and association kinetics – more so than nMag-Gly55Asp. In fact, the nMag-Gly55Ala mutation alone sufficiently improved mitochondrial recruitment after preincubation at 28°C so that it functioned well as a monomer (**Figure 1-figure supplement 3D**).

Thermostabilization of the Magnets proteins

Having improved the system to allow single-copy use at 28°C, we next sought to improve the temperature stability of the proteins to allow experiments at 37°C. As before, recruitment to the mitochondrial membrane in HeLa cells was used as the cellular assay: nMagHigh1-Gly55Ala-EGFP-OMP25 and pMagFast2-TagRFP-T were co-expressed on the outer mitochondrial membrane and in the cytoplasm, respectively, of HeLa cells by co-transfection. Identical amounts of DNA, in the same plasmid ratio, were used, to allow side-by-side quantification of expression level, background association in the dark, heterodimerization efficiency, and kinetics of association and dissociation. Cells were preincubated at 28°C, 33°C, 35°C, or 37°C for 12-24 hours and then imaged at 37°C to quantify mitochondrial accumulation. We made and tested a number of mutants (**Figure 1-figure supplement 3A, Supplementary File 3**) in the assay.

Mutations were designed according to multiple criteria: removal of potential ubiquitination sites, improvement in secondary structure preference, and mutations based on the homologous Vivid domains of the thermophilic ascomycetes *Thielavia terrestris*, *Myceliophthora thermophila*, *Chaetomium thermophile*, *Rhizomucor pusillus*, *Rhizomucor miehei*, *Thermomucor indicae,* and *Thermothelomyces thermophilus* (**Figure 1-figure supplement 4**), which have optimal growth temperatures around 50°C (Oliveira and Rodrigues, 2019). Mutations were introduced into both nMagHigh1-Gly55Ala and pMagFast2 components. A number of single mutations improved dimerization efficiency and/or kinetics upon preincubations at 28°C and higher temperatures (**Supplementary File 3**). Of the individual mutations tested, Thr69Leu, Met179Ile, and Ser99Asn (all from thermophilic homologues) each improved dimerization efficiency at 28°C, and the latter allowed it at 33°C. Thr69Leu is in the interface and improves hydrophobic interactions (**Figure 1-figure supplement 5A,B**), Met179Ile is in the hydrophobic core and improves packing (**Figure 1-figure supplement 5C,D**), and Ser99Asn is surface-exposed and optimizes hydrogen bonding and secondary-structure preference (**Figure 1-figure supplement 5E,F**). Combining these three mutations substantially increased dimerization at both 28°C and 33°C, and all further variants were tested on top of this combination. The mutation Val67Ile increased dimerization efficiency at 33°C; however, it also slowed recovery kinetics – thus, we did not include it. Mutations of Asn133 to lysine or phenylalanine (the latter from thermophiles) both enhanced dimerization at 33°C, with Asn133Phe facilitating it at 35°C, but with slower dissociation kinetics. The additional Tyr94Glu mutation (from thermophiles, improves helical preference) permitted weak dimerization at 37°C with dissociation kinetics comparable to the original Magnets molecules. The adjacent mutations Asn100Arg/Ala101His (from thermophiles, improves helical preference) allowed stronger 37°C dimerization. Finally, Tyr126Phe (from thermophiles, improves helical preference) and Arg136Lys (from thermophiles, improves helical preference, improves electrostatics with FAD cofactor; **Figure 1-figure supplement 5G,H**) further increased dimerization efficiency. During our screening we identified several point mutations that completely abolished the functionality of the pair even upon 28°C incubation, *e.g.* Gly49Ala, Tyr50Phe or Ile, Asn56Thr, Tyr87Phe, Val103Ile, Arg106Lys, Lys125Arg, Asp128Ala or Glu, Asn130Glu, Ile139Leu, Phe162Ile or Leu, Ser178Cys or Phe (See **Supplementary File 3** for details; other mutations worsened performance without abolishing it). These results will help elucidate LOV domain structure-function relationships – particularly in the absence of comprehensive structural characterization of the light-dependent conformational changes in LOV domain dimers.

We selected a pair of variants, eMags, with these nine mutations (Thr69Leu, Tyr94Glu, Ser99Asn, Asn100Arg, Ala101His, Tyr126Phe, Asn133Phe, Arg136Lys, and Met179Ile) added to nMagHigh1-Gly55Ala and pMagFast2. eMags supports dimerization upon growth at 37°C without preincubation at a lower temperature, while the original Magnets variants were completely nonfunctional after these growth conditions (**Figure 1C,D**, **Figure 1-source data 1, Figure 1-figure supplement 6, Figure 1-figure supplement 6-source data 1**). eMags show greater dimerization efficiency (~4-5x), as judged by greater prey accumulation on mitochondria ($p=0.0004$, Kruskal-Wallis and Dunn's multiple comparison *post hoc* tests; **Figure 1D**) and faster association and dissociation kinetics ($\tau^{ON} = 3.6 \pm 0.3$ s, $\tau^{OFF} = 23.1 \pm 0.6$ s) than original Magnets in cells preincubated at 28°C ($\tau^{ON} = 7.6 \pm 0.3$ s, $\tau^{OFF} = 32.0 \pm 1.3$ s; $p < 0.0001$ for both τ^{ON} and τ^{OFF}, unpaired Student's t-test; **Figure 1C**). Omission of the Tyr126Phe mutation in eMags produced eMags^{F}, with similar but slightly lower dimerization efficiency as eMags, but significantly faster association and dissociation kinetics ($\tau^{ON} = 2.8 \pm 0.3$ s, $\tau^{OFF} = 14.0 \pm 0.6$ s; $p < 0.0001$ for both τ^{ON} and τ^{OFF}, unpaired t-test; **Figure 1C**). A 3x prey concatemer (*i.e.* nMagHigh1-EGFP-OMP25 and pMagFast2(3x)-TagRFP-T) – still requiring preincubation at 28°C – is needed to bring the prey recruitment of original Magnets in line with that of monomeric eMags and eMags^{F} (**Figure 1D**). This concatemerized original Magnets also suffers from slower dissociation kinetics ($\tau^{ON} = 5.6 \pm 0.5$ s, $\tau^{OFF} = 45.9 \pm 1.4$ s; $p = < 0.0001$ for both τ^{ON} and τ^{OFF}, unpaired t-test; **Figure 1C,D**). We refer to nMagHigh1-Gly55Ala and pMagFast2 with these nine mutations as eMagA (Acidic heterodimerization interface) and eMagB (Basic heterodimerization interface), respectively.

eMags enables rapid, local and reversible control of protein recruitment to subcellular compartments

We then sought to establish performance of the new eMags constructs in a variety of experimental contexts. In the first, we used eMags to conditionally recruit cytosolic proteins to intracellular organelles other than mitochondria. For the endoplasmic reticulum (ER), we selected the N-terminal transmembrane domain of cytochrome P450 (Szczesna-Skorupa and Kemper, 2000), which displays on the cytoplasmic face of the ER, as bait (fused to EGFP). Co-expression of this construct, ER-EGFP-eMagA, with eMagB-TagRFP-T (prey) in COS7 cells showed large, rapid, reversible accumulation of prey to the ER upon whole-cell illumination (**Figure 2A**, **Figure 1-figure supplement 2B**, and **Video 2**) (See **Figure 1-figure supplement 1A,B**, **Supplementary File 1 and 2**, **Methods** for a complete list and detailed information on bait and prey constructs used in these experiments). With focal illumination,

249 robust prey accumulation occurred only in the irradiated ER region (**Figure 2B** and **Video 3**), in spite of
250 the known rapid diffusion of proteins within the ER network (Nehls et al., 2000).

Figure 2

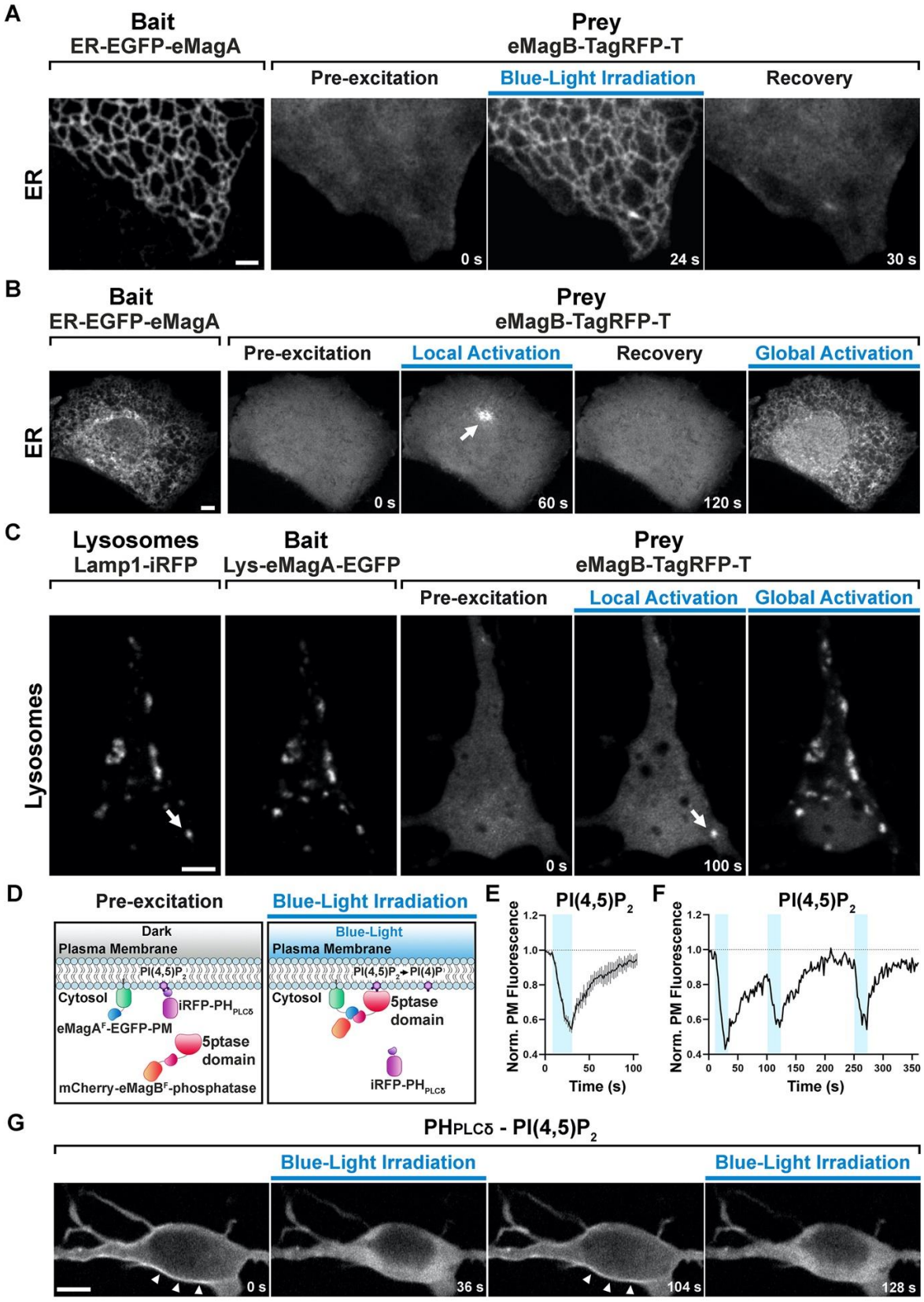
A
Bait
ER-EGFP-eMagA
Prey
eMagB-TagRFP-T
Pre-excitation
Blue-Light Irradiation
Recovery
ER
0 s
24 s
30 s
B
Bait
ER-EGFP-eMagA
Prey
eMagB-TagRFP-T
Pre-excitation
Local Activation
Recovery
Global Activation
ER
0 s
60 s
120 s
C
Lysosomes
Lamp1-iRFP
Bait
Lys-eMagA-EGFP
Prey
eMagB-TagRFP-T
Pre-excitation
Local Activation
Global Activation
Lysosomes
0 s
100 s
D
Pre-excitation
Blue-Light Irradiation
Dark
Plasma Membrane
PI(4,5)P2
Cytosol
iRFP-PHPLCδ
eMagAF-EGFP-PM
5ptase domain
mCherry-eMagBF-phosphatase
Blue-Light
Plasma Membrane
PI(4,5)P2 → PI(4)P
Cytosol
5ptase domain
iRFP-PHPLCδ
E
PI(4,5)P2
Norm. PM Fluorescence
Time (s)
F
PI(4,5)P2
Norm. PM Fluorescence
Time (s)
G
PHPLCδ - PI(4,5)P2
Blue-Light Irradiation
Blue-Light Irradiation
0 s
36 s
104 s
128 s

251

Figure 2: eMags-dependent recruitment of soluble cytosolic proteins to intracellular organelles and modulation of $PI(4,5)P_2$ at the plasma membrane.

A. Rapid, reversible accumulation of a soluble prey to an endoplasmic reticulum-anchored bait upon whole-cell illumination of a COS7 cell. In this and other examples in the figure, global cell blue-light irradiation was achieved with 200 ms blue-light pulses at 0.5 Hz. Time from the beginning of imaging given at the bottom. Scale bar: 2 μm.
B. Localized and global recruitment of a soluble prey to an ER-targeted bait in a HeLa cell. Localized activation was achieved by illuminating the cell within a 3 μm x 3 μm ROI with 200 ms blue-light pulses at 0.5 Hz for 60 seconds. The cell was then allowed to recover in the absence of blue light for 2 min prior to global illumination. Scale bar: 5 μm. C. Recruitment of a soluble prey to lysosomes in a DIV14 primary hippocampal neuron. The left two fields show colocalization of the lysosomally anchored bait with the lysosomal marker Lamp1-iRFP. Recruitment of the prey to a single lysosome, or to all lysosomes, was achieved by local and global illumination, respectively. Following localized illumination delivered as in (B), the cell was allowed to recover in the absence of blue light for 1 min, and then globally illuminated. Scale bar: 5 μm. D. Schematic representation of the strategy and constructs used to induce $PI(4,5)P_2$ depletion at the plasma membrane via the $eMag^F$-dependent recruitment of an inositol 5-phosphatase. iRFP-$PH_{PLC\delta}$ is a $PI(4,5)P_2$ probe.
E. $PI(4,5)P_2$ dephosphorylation and re-phosphorylation elicited in DIV7 primary hippocampal neurons expressing the constructs shown in (D) (N= 10 dephosphorylation and re-phosphorylation events, 3 neurons), as reflected by the dissociation of iRFP-$PH_{PLC\delta}$ from the plasma membrane.
F. Representative trace of $PI(4,5)P_2$ level changes resulting from multiple brief illumination pulses of a single neuron.
G. Selected iRFP-$PH_{PLC\delta}$ images of the neuron used for field (F) at the times indicated. Scale bar: 5 μm.

For recruitment to lysosomes, we used the N-terminal transmembrane sequence of Late Endosomal/Lysosomal Adaptor, MAPK and mTOR Activator 1 (p18/LAMTOR1), the principal lysosomal surface anchor protein for the mTOR pathway (Nada et al., 2014). We co-expressed this bait, Lys-eMagA-EGFP, prey eMagB-TagRFP-T, and lysosomal marker Lamp-1-iRFP in primary mouse hippocampal neurons (14 DIV); focal illumination of single lysosomes drove prey recruitment selectively to these isolated organelles (**Figure 2C** and **Video 4**), demonstrating the excellent spatial precision of eMag photoactivation.

Finally, for recruitment to the plasma membrane (PM), we targeted eMagA^{F}-EGFP bait to the cytoplasmic PM face with the CAAX-box membrane-targeting sequence from N-ras (Choy et al., 1999). As bait, we used mCherry-eMagB^{F} for fluorescence visualization, and also fused the catalytic domain from the inositol 5-phosphatase OCRL (Pirruccello and Camilli, 2012), which dephosphorylates phosphatidylinositol 4,5-bisphosphate (PI(4,5)P_2). To monitor the degradation of PI(4,5)P_2 by the recruited OCRL, we expressed a third fluorescent protein, iRFP, fused to the Pleckstrin homology (PH) domain of phospholipase-Cδ1 ($PH_{PLC\delta}$), which selectively binds PI(4,5)P_2 over other lipid head groups (Hammond and Balla, 2015) and thus serves as a localization sensor for PI(4,5)P_2. All three constructs were co-expressed in primary hippocampal neurons (7 DIV). Blue-light irradiation of cells induced rapid accumulation of TagRFP-T signal at the PM (reflecting OCRL recruitment) and subsequent iRFP signal loss from the PM (reflecting OCRL activity converting PI(4,5)P_2 to phosphatidylinositol 4-phosphate (PI4P) and subsequent $PH_{PLC\delta}$ release to the cytoplasm; **Figure 2D-G** and **Video 5**). iRFP signal rapidly decayed (τ^{ON} = 18.1 ± 4.6 s) to half its initial level (~30 s) indicating rapid eMag binding, OCRL activity, and $PH_{PLC\delta}$ unbinding. Upon interruption of blue light irradiation, the iRFP signal quickly recovered (τ^{OFF} = 23.4 ± 1.6 s), indicating fast eMag unbinding, PI(4,5)P_2 resynthesis, and $PH_{PLC\delta}$ binding (yielding iRFP signal recovery) (**Figure 2E**, **Figure 2-source data 1)**. Importantly, multiple cycles of illumination produced essentially identical waveforms of iRFP signal and recovery to initial levels, showing that both eMag binding and unbinding, and PI(4,5)P_2 generation, are readily reversible with little drift from baseline (**Figure 2F**).

Optogenetic regulation of inter-organellar contacts

In another set of applications, we validated the efficiency of eMags to induce organelle contacts (**Figure 3A, Figure 1-figure supplement 1D**). Conditional induction or expansion of such contacts may help elucidate the contribution of inter-organelle contacts and signaling to a variety of biochemical pathways.

We first designed a light-inducible ER-lysosome tethering system. Using the targeting sequences above (**Figure 2**), ER-mCherry-eMagA and Lys-eMagB-iRFP were co-transfected into COS7 cells. Before blue light activation, ER-lysosome overlap, as detected by mCherry and iRFP overlap, was minimal (**Figure 3B**); during 1 min. irradiation, colocalization rapidly increased by ~50% (τ^{ON} =7.5 ± 0.8 s, N=14 cells, 3 independent experiments, **Figure 3-source data 1**), most likely through expansion of pre-existing contacts or by stabilization and expansion of new contacts. Following light offset, ER-lysosome colocalization declined quickly to baseline (τ^{OFF} = 35.9 ± 1.7 s; **Figure 3B**, **Video 6**). The longer time courses of organelle association-dissociation (tens of seconds), relative to cytoplasmic protein recruitment (seconds), is consistent with a combination of slower mobility of organelles than free protein and the processive assembly and disassembly of membrane contacts.

Using a similar targeting strategy, ER-mCherry-eMagA and eMagB-iRFP-Mito were used to drive ER-mitochondrial association (**Figure 3C**). In HeLa cells, used for these experiments, ER and mitochondria form a closely interacting network even in control conditions. Upon 2 min. irradiation, however, overlap increased by ~20%, with kinetics (τ^{ON} = 28.0 ± 1.9 s, τ^{OFF} = 49.1 ± 2.5 s, N=14 cells, 3 independent experiments; **Figure 3C, Video 7, Figure 3-source data 1**) on the order of that seen for ER-lysosome contacts.

Finally, for mitochondrion-lysosome manipulation, we used eMagA-mCherry-Mito and Lys-eMagB-iRFP. In HeLa cells, baseline colocalization was quite low (**Figure 3D**); such contacts are typically transient and involve small contact area (Wong et al., 2018). Upon activation, increased associations between lysosomes and mitochondria were observed, revealing contact expansion (τ^{ON} = 40.1 ± 2.6 s, τ^{OFF} = 58.4 ± 2.6 s, N=17 cells, 3 independent experiments; **Video 8, Figure 3-source data 1**). In some cases, movement of lysosomes away from mitochondria resulted in the elongation of tubules from mitochondria, and even in their fission (**Figure 3E, Video 9**), indicating strong association.

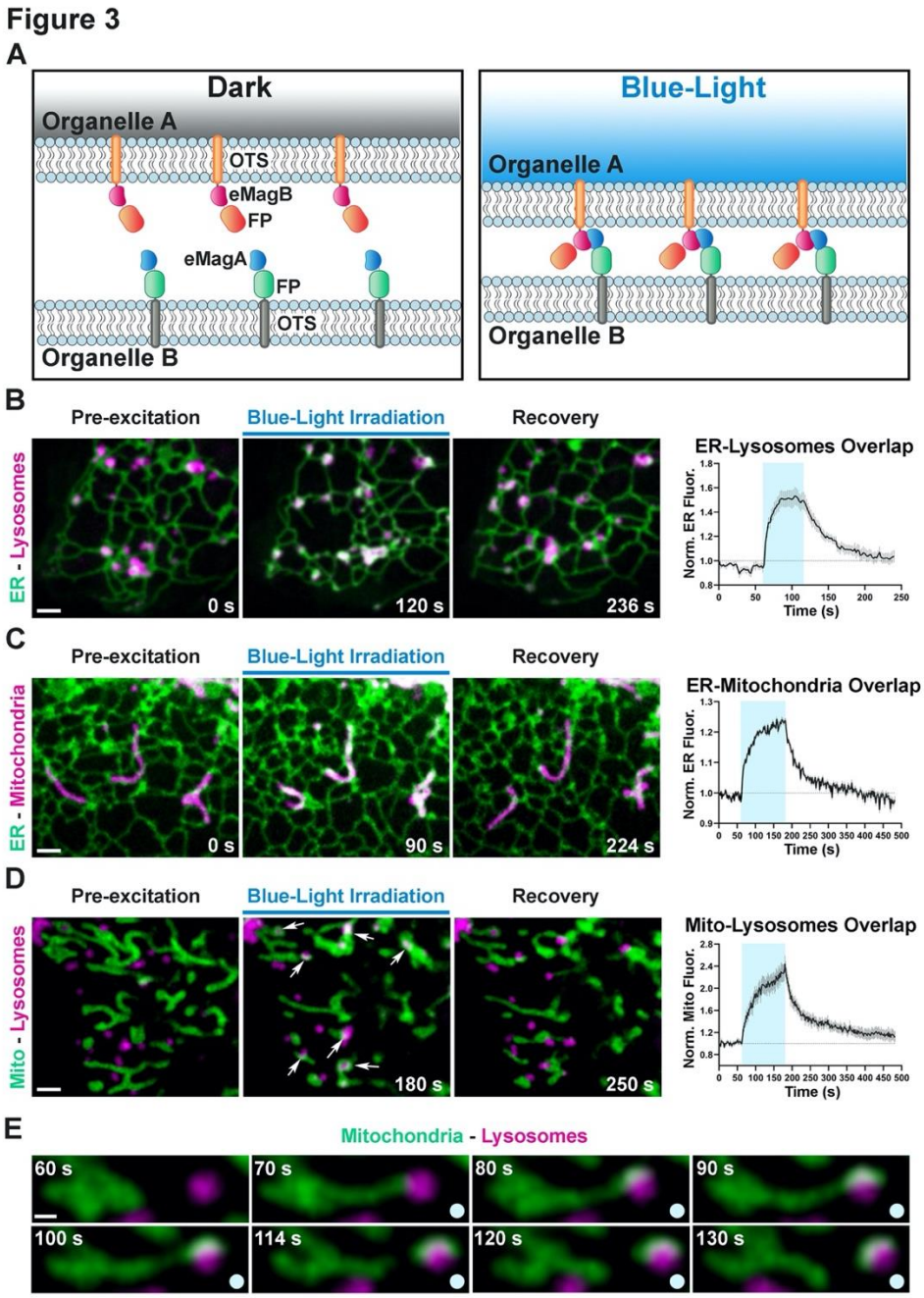

Figure 3: Optogenetic induction of organelle-organelle contacts

A. Graphical representation of the strategy used to establish contacts between membranes of intracellular organelles. Constructs encoding both components of the dimerization pair (eMagA and eMagB) were fused to a fluorescent protein (FP) and to an organelle-targeting sequence (OTS) to drive expression in specific organelles (Organelle A or B). Cells expressing, respectively: ER-Lysosomes (COS7) (B), ER-Mitochondria (HeLa) (C), or Mitochondria-Lysosomes (HeLa) (D). Cells shown before, during, and after blue-light illumination. Small arrows in (D) point to lysosomes. The overlap between the membranes of the two organelles increased during illumination, as illustrated by the white color in the fluorescence micrographs, quantified in graphs shown at right (ER-Lysosomes: n = 14, ER-Mitochondria: 14, Mito-Lysosomes: 17; 3 independent experiments). Scale bar: 2 µm.

E. Fission of a mitochondrion correlating with pulling by a lysosome after light-dependent contact formation/expansion. Scale bar: 0.5 µm.

Control of the PI4P Golgi pool by reconstitution of VAP (Opto-VAP)

In a final application, we tested eMags for acute manipulation of intracellular PI4P *via* reconstitution of an ER-transGolgi network (TGN) tether. Key components of this tether are the ER protein VAMP-associated protein (VAP) and Oxysterol-binding protein 1 (OSBP1). OSBP1, which binds VAP (*via* an FFAT motif) and membranes of the TGN (*via* a PI4P-binding PH domain), also contains an ORD domain (OSBP-related domain) that promotes exchange of TGN PI4P for ER cholesterol (Murphy and Levine, 2016). Following shuttling to the ER, PI4P is degraded by the phosphatidylinositide phosphatase Sac1 (Mesmin et al., 2013; Saint-Jean et al., 2011; Zewe et al., 2018). This model of ER-Golgi PI4P transport is supported by biochemical, pharmacological, and genetic studies (Dong et al., 2016; Mesmin et al., 2013; Strating et al., 2015). We sought to use the eMags tools to offer direct optogenetic control over this PI4P-cholesterol exchange through regulation of VAP-OSBP1 binding interactions.

The overall design strategy was to replace endogenous VAP with a split version, which could be reconstituted by eMag dimerization and would then associate with OSBP1 to drive transport. Unlike the earlier examples, this necessitated careful consideration of the domain architectures of VAP and OSBP1, to best ensure that 1) split-VAP would not reconstitute in the absence of light activation and 2) that the eMagA and eMagB fusions would not interfere with either VAP reconstitution or OSBP1 interaction. VAP is an integral membrane protein composed of a cytosolic major sperm protein (MSP) domain (which binds FFAT motif-containing proteins), a coiled-coil domain and a C-terminal membrane anchor (Kaiser et al., 2005; Kim et al., 2010) (**Figure 4A** and **Figure 1-figure supplement 1E**). Two distinct VAP genes exist in the vertebrate genome: VAPA and VAPB, which can form either homomers or heteromers with one another. OSBP1 has an N-terminal PH domain that preferentially binds PI4P (Mesmin et al., 2013; Murphy and Levine, 2016; Venditti et al., 2019), an internal FFAT motif, and a C-terminal ORD domain which binds in a competitive way PI4P and cholesterol. Given this domain structure, we opted to convert VAPB into a cytosolic version through deletion of the C-terminal transmembrane helix (leaving $VAPB_{(1-218)}$); we retained the MSP and coiled-coil domains as both may contribute to VAP dimerization (Kim et al., 2010) (**Figure 4B**). We fused TagRFP-T to the N-terminus of this cytosolic fragment, and eMagB to its C-terminus (TagRFP-T-$VAPB_{(1-218)}$- eMagB; **Figure 4B, Figure 1-figure supplement 1E** and **Supplementary File 2**). We then used ER-eMagA-EGFP to recruit $VAPB_{(1-218)}$ to the ER upon blue light irradiation, where it could interact with OSBP1. We refer to this pair of constructs as "Opto-VAP".

Figure 4

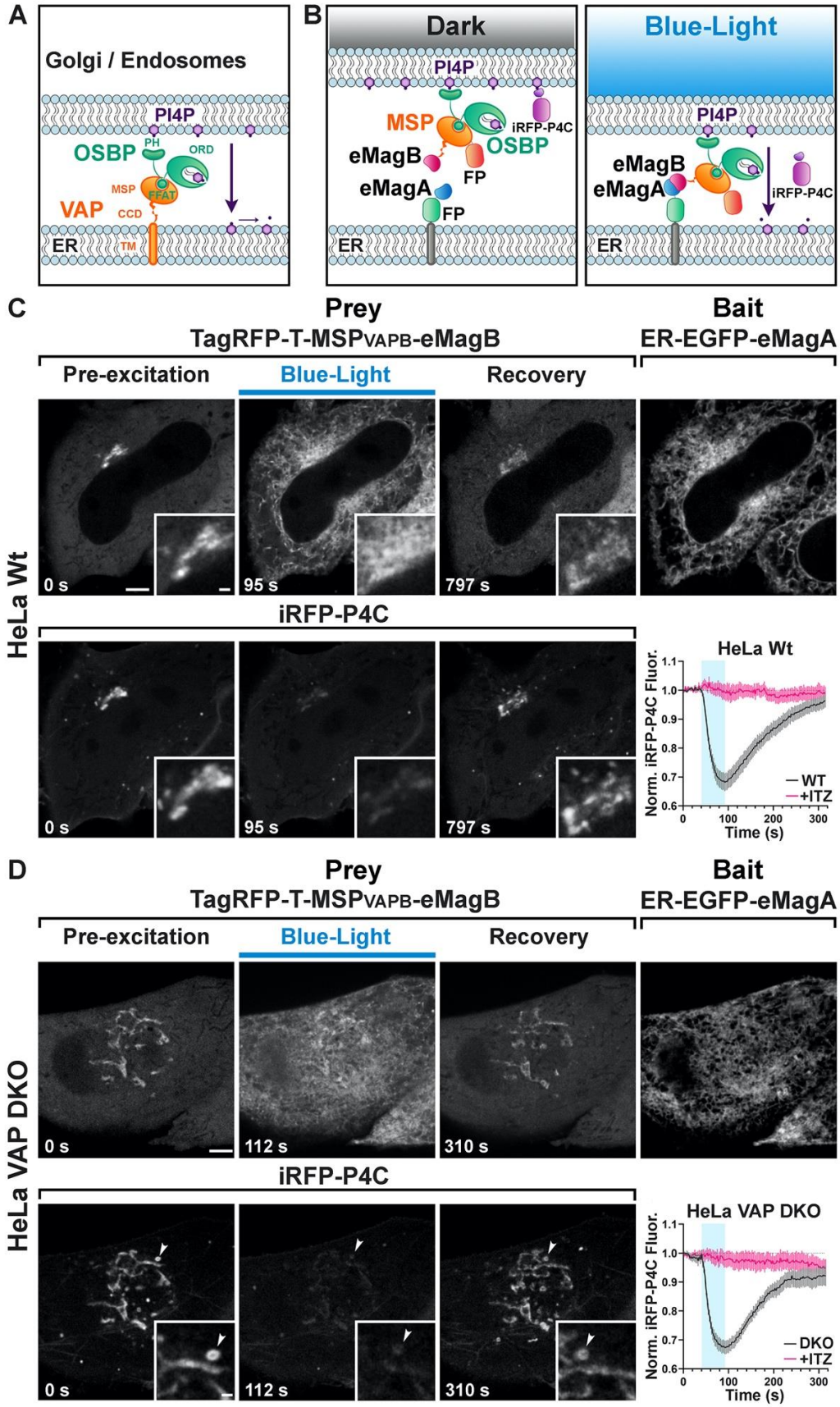
A
Golgi / Endosomes
PI4P
OSBP
PH
ORD
MSP
FFAT
VAP
CCD
ER
TM
B
Dark
Blue-Light
PI4P
MSP
iRFP-P4C
OSBP
eMagB
FP
eMagA
FP
ER
PI4P
eMagB
eMagA
iRFP-P4C
ER
C
Prey
TagRFP-T-MSPVAPB-eMagB
Bait
ER-EGFP-eMagA
Pre-excitation
Blue-Light
Recovery
HeLa Wt
0 s
95 s
797 s
iRFP-P4C
0 s
95 s
797 s
HeLa Wt
Norm. iRFP-P4C Fluor.
1.1
1.0
0.9
0.8
0.7
0.6
0
100
200
300
Time (s)
WT
+ITZ
D
Prey
TagRFP-T-MSPVAPB-eMagB
Bait
ER-EGFP-eMagA
Pre-excitation
Blue-Light
Recovery
HeLa VAP DKO
0 s
112 s
310 s
iRFP-P4C
0 s
112 s
310 s
HeLa VAP DKO
Norm. iRFP-P4C Fluor.
1.1
1.0
0.9
0.8
0.7
0.6
0
100
200
300
Time (s)
DKO
+ITZ

393

Figure 4: Light-dependent reconstitution of VAPB triggers PI4P transfer from the Golgi complex and endosomes to the ER

A. Domain organization of VAP and OSBP1, which together connect the ER to the PI4P-rich membranes of the Golgi complex (and an endosome subpopulation) to mediate PI4P transfer to the ER for degradation by the PI4P phosphatase Sac1. MSP: major sperm protein homology domain; CCD, coiled-coil domain; TM, transmembrane domain; PH, Pleckstrin homology domain; FFAT, FFAT motif; ORD, OSBP-related protein lipid-binding domain. In the experiment shown in the figure, OSBP represents the endogenous protein.

B. Schematic representation of reconstitution of a split VAP on the ER membranes using eMags (Opto-VAP). FP: fluorescent protein tags. The N-terminal portion of VAPB ($VAPB_{(1-218)}$) fused to TagRFP-T and to eMagB (prey) was expressed together with ER-anchored eMagA fused to EGFP (bait) and with the PI4P reporter iRFP-P4C in HeLa cells. Upon blue-light illumination, eMags heterodimer formation results in reconstitution of the tether, allowing the ORD domain of endogenous OSBP to transfer PI4P to the ER for degradation, leading to PI4P loss from Golgi membranes.

C. Wild-type HeLa cell expressing TagRFP-T-MSP($VAPB_{(1-218)}$)-eMagB, ER-EGFP-eMagA and the PI4P reporter iRFP-P4C, showing that blue-light dependent Opto-VAP activation results in the recruitment of the prey to the ER and concomitant dissociation of iRFP-P4C from the Golgi, reflecting PI4P loss. Scale bar: 5 µm. Insets show the Golgi complex area at higher magnification. Scale bar: 1 µm. The graph at bottom-right shows changes of normalized iRFP-P4C (PI4P) fluorescence in the Golgi complex before, during, and after Opto-VAP activation in wild-type HeLa cells, with or without ITZ treatment (N=16 and 24 cells, respectively; from 3 independent experiments).

D. VAP-DKO HeLa cell expressing the same constructs as in (C). As previously reported (Dong et al. 2016), in VAP-DKO HeLa cells, the Golgi complex is disrupted with an accumulation of PI4P-rich hybrid endosome-Golgi organelles. Blue-light dependent Opto-VAP activation results in the prey recruitment to the ER and concomitant dissociation of iRFP-P4C from these organelles. Scale bar: 5 µm. Insets of the iRFP-P4C images of Golgi-endosome elements at high magnification. The bright vesicular structure shown in the inset corresponds to the organelle indicated by an arrowhead in the low magnification image. Scale bar: 1 µm. The graph at bottom-right shows changes of normalized iRFP-PI4C (PI4P) fluorescence in endosomes before, during, and after Opto-VAP activation, with or without ITZ treatment (N=20 and 16, respectively; from 3 independent experiments).

We first tested the efficiency of Opto-VAP by transfecting both components into HeLa cells and imaging them by confocal microscopy. The prey protein (TagRFP-T-VAPB$_{(1-218)}$-eMagB) was imaged throughout the experiment, while ER-eMagA-EGFP was imaged only during optogenetic activation. Before blue light irradiation, the prey protein was homogeneously distributed throughout the cytosol, with focal accumulation around the Golgi (**Figure 4C**). We interpret this observation as reflecting interaction of VAPB with endogenous OSBP1, which is abundant in the Golgi, where it binds the PI4P-rich TGN membranes *via* its PH domain (Mesmin et al., 2013). The cytosolic VAPB$_{(1-218)}$ prey, with its MSP domain, could compete with endogenous VAP for binding to the FFAT motif of OSBP1 (**Figure 4A,B**). A robust presence of PI4P in the TGN under resting conditions was confirmed by strong colocalization with co-transfected PI4P reporter iRFP-P4C (Hammond and Balla, 2015; Luo et al., 2015) (**Figure 4C**). Upon irradiation with blue light (50 ms blue-light pulses at 0.5 Hz for ~1 min.), there was a massive recruitment of TagRFP-T-VAPB$_{(1-218)}$-eMagB to the ER (**Figure 4C**-top, **Figure 4-figure supplement 1, 2A**), consistent with VAP-OSBP1-based reconstitution of ER-TGN interactions. Concomitant with this was a rapid (τ^{ON} = 22.8 ± 2.4 s) reduction of iRFP fluorescence in the Golgi (**Figure 4C**-bottom**, Video 10, Figure 4-source data 1**), approaching a plateau of ~70% of resting in approximately 50 s. This suggests that optogenetic reconstitution of split-VAP indeed restores a VAP-OSBP1-dependent ER-TGN tether and resulting transport of PI4P from the Golgi to the ER. These changes were rapidly reversed after interruption of blue light, with the full regeneration of the PI4P signal to baseline occurring in approximately 5 minutes (τ^{OFF} = 143.8 ± 3.8 s).

To confirm that the observed PI4P transfer was indeed mediated by OSBP and Opto-VAP, cells were preincubated for 30 min with 10 μM itraconazole (ITZ), an antifungal and anticancer agent that occludes the lipid-transport domain of OSBP and thus blocks its lipid trafficking properties (Strating et al., 2015). After ITZ treatment, no change was detected in the accumulation of the PI4P probe (iRFP-P4C) at the Golgi (graph in **Figure 4C** and **Figure 4-figure supplement 1, 2A, Figure 4-source data 1, Figure 4-figure supplement 2-source data 1**), despite the efficient recruitment of TagRFP-T-VAPB$_{(1-218)}$-eMagB to the ER membrane (N=16 cells, 2 independent experiments).

We next tested the Opto-VAP system in gene-edited HeLa cells lacking both VAP genes (VAP double-KO cells). It was reported that in these cells the Golgi complex is partially disrupted, with formation of PI4P-enriched hybrid Golgi-endosome structures (Dong et al., 2016), a finding that we have confirmed

in cells kept in the dark (**Figure 4D**-bottom). Blue light activation led to rapid recruitment of TagRFP-T-VAPB$_{(1-218)}$-eMagB to the ER (**Figure 4-figure supplement 2B**), whose reticular appearance was less obvious in these cells (**Fig. 4D**-bait panel) due their greater thickness relative to the COS7 cells used in other experiments. Concomitant with VAPB$_{(1-218)}$ recruitment to the ER, rapid (τ^{ON} = 15.7 ± 1.2 s) decrease in iRFP fluorescence from the Golgi and hybrid Golgi-endosome structures was observed (**Figure 4D**, **Figure 4-source data 1** and **Video 11**), indicating PI4P loss. Thus, Opto-VAP is able to fully restore the activity of the deleted VAPA and VAPB genes in recruiting OSBP1 to perform PI4P-cholesterol exchange. After blue-light interruption, both Opto-VAP localization and PI4P levels reversed to baseline (τ^{OFF} = 93.7 ± 5.0 s) (**Figure 4D**) (N=20 cells, 4 independent experiments). As before, ITZ completely inhibited PI4P transport but had no effect on Opto-VAP recruitment (N=16 cells, 3 independent experiments) (**Figure 4D, Figure 4-source data 1**, **Figure 4-figure supplement 2B, Figure 4-figure supplement 2-source data 1**). The time courses of Opto-VAP recruitment and recovery, and of PI4P loss and recovery, are similar between the wild-type and double-KO cells, suggesting that Opto-VAP assembly and function are largely independent of endogenous levels of VAPA and VAPB.

As a final verification of the necessity of the ORD domain in the observed PI4P transport, we constructed TagRFP-T-eMagB-PH$_{OSBP}$, with the PH domain of OSBP1 but not the ORD domain (**Figure 4A**, **Figure 1-figure supplement 1E, Figure 4-figure supplement 3A a**nd **Supplementary File 2**). In both wild-type or VAP-DKO HeLa cells, blue-light activation induced rapid prey recruitment to the ER, but with no accompanying changes in iRFP-P4C fluorescence (**Figure 4-figure supplement 3B,C** and **Figure 4-figure supplement 3-source data 1**; n=16 cells for HeLa, n=17 for VAP-DKO, 2 independent experiments). Thus, the ORD domain is critical for PI4P transport, with the PH domain alone having no effect.

DISCUSSION

In this work, we have both engineered a dramatically improved photodimerizer pair and used it in a set of experiments elucidating details of organellar interactions and cellular lipid metabolism and transport. In a previous study (Benedetti et al., 2018), we had compared multiple optogenetic dimerizer reagents and found that the Magnets system, based on orthogonalization of the Vivid LOV domain homodimer (Kawano et al., 2015), offers major advantages over other systems in several different assays. Magnets

have rapid association and dissociation kinetics and require both monomers to undergo blue-light activation to permit dimerization. These properties make the background activation of Magnets low, so that they are well-suited to optogenetic modulation of small volumes and sub-cellular organelles. However, the existing Magnets tools have two critical disadvantages, which preclude their wider adoption: 1) their weak dimerization efficiency necessitates the use of concatemers, which can perturb target proteins and slow kinetics, and 2) the low thermodynamic stability means that expression and maturation must occur at reduced temperatures, complicating cell culture experiments and ruling out mammalian *in vivo* work entirely.

To overcome these limitations, we established a robust cell-culture screen that captures dimerization efficiency, association and dissociation kinetics, and folding and maturation. This screen allowed us to identify variants encompassing mutations across the whole protein with particular focus on the dimer interface. Mutations were selected based on sequence alignments with thermophilic fungal Vivid domains and structure-guided design. After several rounds of mutagenesis and screening, we selected final "enhanced Magnets" (eMag) variants with nine mutations over the starting scaffolds. The eMag reagents showed greater dimerization efficiency – allowing use as monomers instead of concatemers, full function after their folding and maturation at 37^{o}C, and faster association and dissociation kinetics than the original Magnets.

We recently compared (Benedetti et al., 2018) the original Magnets system to Cry2/CIB1 (Kennedy et al., 2010) and iLIDs (Guntas et al., 2014), using several of the assays also used in this study, e.g. protein recruitment to ER, mitochondria, or single lysosomes, and activity of OCRL phosphatase recruited to the plasma membrane. From this systematic comparison, several obvious themes emerged. Firstly, upon prolonged local (3 μm x 3 μm) illumination, Magnets dimerization occurs and persists only in the irradiated region, while activated iLID dimers extend some distance from this region and activated Cry2/CIB1 dimers penetrate the entire cell. Secondly, recovery kinetics of Cry2/CIB1 after light offset are more than an order of magnitude slower than those of iLIDs and Magnets. Thirdly, the efficiency of light-driven recruitment of original Magnets is greater than that of iLIDs but somewhat lower than that of Cry2/CIB1. Importantly, use of Cry2/CIB1 involves a balance between the desired Cry2/CIB1 heterodimerization and counterproductive Cry2 oligomerization (Bugaj et al., 2013; Che et al., 2015; Duan et al., 2017; Taslimi et al., 2016). This balance is difficult to determine and could vary across

cellular environments and target proteins. Finally, Cry2 is less effective when used in membrane-bound bait (Benedetti et al., 2018; Che et al., 2015; Hallett et al., 2015; Pathak et al., 2014), hampering its utility in applications such as those shown here (Cry2 is much larger than LOV domains and may perturb fused proteins and organelles). Relative to the original Magnets – which we systematically compared to Cry2/CIB1 and iLIDs in our previous study – eMags shows significant improvements in the dimerization efficiency, and association and dissociation kinetics. Taken together, eMags provides several advantages over Cry2/CIB1 and iLIDs for subcellular optogenetics and perhaps other settings as well.

We have shown the benefits of the faster eMag^{F} clones for rapid manipulation. In the other direction, it is likely that grafting the photoactivation-extending mutations Val74Ile and/or Val85Ile (Zoltowski et al., 2009) could produce high-efficiency, thermostable versions of eMags with recovery kinetics on the order of minutes to hours, if experimenters desire bistable control of protein-protein interactions.

We thoroughly validated the eMags constructs in a range of cellular assays both in whole cell and local irradiation conditions involving protein recruitment to different membranes, inter-organellar association, and bilayer lipid metabolism and trafficking. The success of the engineering effort validates the design strategy and shows that many mutations from thermophilic fungi grafted well to the scaffold of the Vivid photoreceptor of *Neurospora crassa,* a mesophilic fungus. These mutations improved packing, hydrogen bonding, and secondary structure preference. These improved optogenetic dimerizers will be broadly applicable and useful for applications across diverse fields. Also, our protein design and cellular screening strategies will likely extend to other reagent optimization projects.

MATERIALS AND METHODS:

Plasmids

Expression vectors encoding nMagHigh1-EGFP-CAAX, pMagFast2(3x)-iRFP and iSH2-pMag(3x)-iRFP were kind gifts from Moritoshi Sato (University of Tokyo, Tokyo, Japan). nMagHigh1-EGFP-Mito was generated through the PCR amplification of the nMagHigh1-EGFP coding sequence from nMagHigh1-EGFP-CAAX and inserted into a pGFP-OMP25 (Nemoto and Camilli, 1999) vector at NheI and XhoI sites. pMagFast2(1x)-TagRFP-T was generated through the PCR amplification of the third unit of pMagFast2(3x) and TagRFP-T in pMagFast2(3x)-TagRFP-T (Benedetti et al., 2018) and inserted in the same vector at HindIII and XbaI site. In order to recreate an optimal Kozak sequence Met and Gly were added before the initial His, at the N-term of pMagFast2 in this construct. All nMagHigh1 and pMagFast2 mutants tested in our screening were generated by site-directed mutagenesis (QuikChange II XL, Agilent technologies) following manufacturer instruction. The complete list of primers can be found in **Supplementary Files 4, 5**. The sequences of the enhanced Magnets mutants generated have been deposited in Genebank: eMagA^{F} (GenBank accession number: MW203024), eMagB^{F} (GenBank accession number: MW203025), eMagA (GenBank accession number: MW203026), eMagB (GenBank accession number: MW203027). ER-EGFP-eMagA, ER-mCherry-eMagA, eMagA-mCherry-Mito, eMagB-iRFP-Mito, Lys-eMagB-iRFP and TagRFP-T-VAPB$_{(1-218)}$-eMagB were generated by GeneScript and cloned into M18 pCAGGS WPRE electroporation vector (Gray et al., 2006). These constructs are described in **Supplementary File 1 and 2**. Lys-eMagA-EGFP was generated replacing nMagHigh1 with eMagA in Lys-nMagHigh1-EGFP (Benedetti et al., 2018). Lamp1-iRFP was generated by PCR-amplifying the *Homo sapiens* lysosomal associated membrane protein 1 (LAMP1) coding sequence (NCBI Reference Sequence: NM_005561.3) synthetized as a gBlocks® Gene Fragment (Integrated DNA Technologies, IDT), which was inserted at EcoRI and BamHI sites of piRFP670-N1 (Addgene plasmid # 45457). eMagA^{F}-EGFP-PM was generated replacing nMagHigh1 in nMagHigh1-EGFP-CAAX with the engineered variant at HindIII and XbaI sites. mCherry- eMagB^{F} -5ptase$_{OCRL}$ was synthetized by digesting mCherry-pMagFast2(3x)-5ptase$_{OCRL}$ (Benedetti et al., 2018) with NotI and PvuI, and then ligated with eMagB^{F} amplified from eMagB^{F}-TagRFP-T. iRFP-PH$_{PLC\delta}$ plasmids were previously described (Idevall-Hagren et al., 2012). TagRFP-T-eMagB-PH$_{OSBP}$ coding sequence was synthetized as a gBlocks® Gene Fragment (Integrated DNA Technologies, IDT) and cloned into TagRFP-T-VAPB$_{(1-218)}$-eMagB vector at NotI and HpaI cloning

sites. PH_{OSBP} sequence was obtained from GFP-PH_{OSBP} (Tim Levine, UCL Institute of Ophthalmology). iRFP-P4C was cloned amplifying the iRFP coding sequence piRFP670-N1 (Addgene plasmid # 45457) and inserted at AgeI and BsrGI cloning sites in GFP-$P4C_{SidC}$ (kind gift of Yuxin Mao, Cornell). For all of these clones, PCR amplification of the fragments, and their subsequent ligation, was performed using the In-Fusion Cloning Kit and online tools (BD Clontech, Takara Bio, USA). All plasmids were verified by sequencing (Genewiz, South Plainfield, NJ, USA).

Bioinformatics and protein design

Thermophilic Vivid domain homologues were found using tblastn of the *Neurospora crassa* sequence against whole-genome sequences of thermophilic fungi whose identities were found from literature search. Only the closest homologue from each genome was selected for analysis. Several sequences were incomplete, *e.g.* the two *Rhizomucor* homologues. The homologues showed a high level of identity and similarity to the *Neurospora crassa* sequence, with a number of positions that clustered amongst some or all of the thermophilic sequences, but were different from the *Neurospora crassa* sequence (**Figure 1-figure supplement 4**). These were preliminary considered to be promising sites for mutagenesis. Structural analysis was performed on the 3RH8 PDB file (annotated as the "light-state dimer" of Vivid) overlaid with that of 2PD7 ("dark-state monomer") – structures were examined, and images made, with PyMOL 2.3.5.

Primary attention was paid to the dimer interface, the FAD binding site, and surrounding regions. Potentially stabilizing mutations were selected from side-chains that would improve secondary structure preference (e.g. https://bmrb.io/referenc/choufas.shtml), hydrophobic exposure, backbone stabilization, or packing – or from side-chains represented at the corresponding position of the thermophilic sequences. Often these were one and the same. Judgments about packing, exposure, backbone stabilization, and clashes were made using the "Mutagenesis" functionality in PyMOL and analysis with the MolProbity server (http://molprobity.biochem.duke.edu). Ubiquitination was predicted using http://bdmpub.biocuckoo.org/prediction.php. Prioritization of mutations to combine was done considering both proximity in space and in linear sequence (i.e. ability to be encoded on a single primer).

Cell culture

Wild-type (ATCC® CCL-2™) and VAP double KO (DKO) (Dong et al., 2016) HeLa cells, as well as COS7 (ATCC® CRL-1651™)cells, were cultured at 37°C (5% CO_2) in phenol red-free Dulbecco's Modified Eagle Medium (DMEM, Life Technologies), supplemented with 10% fetal bovine serum (Life Technologies), 1 mM sodium pyruvate (Life Technologies), 100 U/ml penicillin, 100 μg/ml streptomycin (Life Technologies), MEM-Non-Essential Amino Acids (Life Technologies), and 1 mM L-glutamine (Life Technologies). All lines were tested monthly and verified as being mycoplasma-free (MycoSensor PCR Assay Kit, Agilent Technologies).

Primary cultures of hippocampal neurons were generated from mouse brains. Hippocampi of P0-P2 C57BL/6 (Charles River) pups were dissected in cold Hank's Balanced Salt Solution [HBSS 1x supplemented with 10 mM HEPES pH 7.4, 100 U/ml penicillin, 100 μg/ml streptomycin, and 1 mM sodium pyruvate (all reagents from Life Technologies)]. Cells were then dissociated by tissue trituration and papain treatment [20U/ml papain (Worthington Biochemical corporation), and 0.2 mg/ml L-cysteine (Sigma) in HBSS, pH 7.4] at 37°C for 15 minutes. Live, dissociated cells (Trypan Blue exclusion) were counted and seeded in plating medium [Neurobasal supplemented with 5% fetal bovine serum, 1% Glutamax, and 2% B27 (all reagents from Life Technologies)] at 3.4 x 10^4 cells/cm^2 on poly-D-lysine-coated (Sigma), glass-bottomed Petri dishes (MatTek corporation). Three hours after transfection, the serum-based medium was replaced with serum-free neuronal medium, and cells were maintained in vitro at 37°C and 5% CO_2. Transient transfection was performed between 4 to 14 days in vitro (DIV). All experimental procedures involving the use of mice were performed in agreement with the Yale University Institutional Animal Care and Use Committee (IACUC) (protocol number 2018-07422), and with the Janelia Farm Research Campus Institutional Animal Care and Use Committee and Institutional Biosafety Committee (protocol number 18-173).

Transient transfection and live cell imaging

For live-cell imaging experiments, cells were seeded on glass-bottomed dishes (MatTek corporation) coated with 0.005 mg/ml human plasma fibronectin (EMD Millipore) at 37°C for 30 minutes, and then washed three times with sterile water. Fibroblastic cells were seeded at a concentration of 10-15 x 10^4 cells/cm^2 per dish and transfected after 24 hours with Lipofectamine 2000 (Life Technologies), following the manufacturer's instructions.

To study prey-protein recruitment at mitochondria during mutant screening, cells were transfected with cDNAs encoding nMagHigh1-EGFP-Mito (bait) and pMagFast2-TagRFP-T (prey) variants at a 1:1 ratio in OptiMEM-I (Thermo Fisher Scientific) (1:4 DNA: lipofectamine ratio). Cells were incubated with the transfection mix for 1 hour. Subsequently, the serum-free medium was replaced by complete DMEM, and cells were incubated at 28°C, 33°C, 35°C or 37°C for 12-24 hours before imaging. All imaging experiments were performed at 37°C in Live-cell imaging solution (Life Technologies). Single-lysosome prey recruitment was performed in 14 DIV hippocampal neurons transfected with Lys-eMagA-EGFP (bait), eMagB-TagRFP-T (prey), and Lamp1-iRFP (reporter) at a 3:2:1 ratio, with 1.5 μg total DNA (1:4 DNA: lipofectamine ratio). Plasma membrane modulation of $PI(4,5)P_2$ was tested in 7 DIV hippocampal neurons transfected with $eMagA^F$-EGFP-PM (bait), mCherry-$eMagB^F$-$5ptase_{OCRL}$ (prey), and iRFP-$PH_{PLC\delta}$ (reporter) at a 3:2:1 ratio, with 1.5 μg total DNA (1:4 DNA: lipofectamine ratio). To study prey-protein recruitment at the ER, cells were transfected with cDNAs encoding ER-eMagA (bait) and eMagB-TagRFP-T (prey) at a 2:1 ratio in OptiMEM-I (Thermo Fisher Scientific) (1:4 DNA: lipofectamine ratio). Light-dependent VAPB reconstitution on ER membranes or PH_{OSBP}-mediated tethering was performed by transfecting wild-type or VAP-DKO HeLa cells with ER-EGFP-eMagA (bait) and TagRFP-T-$VAPB_{(1-218)}$- eMagB or TagRFP-T-eMagB-PH_{OSBP} (prey) and iRFP-P4C at a 3:2:1 ratio in OptiMEM-I (Thermo Fisher Scientific) (1:4 DNA: lipofectamine ratio). In this case, cells were incubated with the transfection mix for 1 hour. Subsequently, the serum-free medium was replaced by complete DMEM with no phenol red, and imaging was performed in the same medium between 16 and 28 hours after transfection. Itraconazole (Tocris, Cat. No. 5981) was dissolved in DMSO to generate a 2 mM solution right before the experiment and diluted in the cell medium at 10 μM final concentration 30 minutes before imaging in a dark room.

Light-dependent induction of contacts between ER and lysosomes was achieve transfecting COS7 cells with ER-mCherry-eMagA and Lys-eMagB-iRFP at a 2:1 ratio in OptiMEM-I (1:4 DNA: lipofectamine ratio). ER-mitochondria contacts were elicited in HeLa cells transfected with ER-mCherry-eMagA and eMagB-iRFP-Mito at a 1:1 ratio in OptiMEM-I (1:4 DNA: lipofectamine ratio). Mitochondria-lysosome contacts were evoked in HeLa cells transfected with eMagA-mCherry-Mito and Lys-eMagB-iRFP. Cells were incubated with the transfection mix for 1 hour. Subsequently, the serum-free medium was replaced by complete DMEM with no phenol red, and imaging was performed in the same medium

between 16 and 28 hours after transfection.

Confocal microscopy

All optogenetic experiments, with the exception of the experiments with Opto-VAP and its controls and the light-dependent induction of inter-organellar contacts, were performed using the Improvision UltraVIEW VoX system (Perkin Elmer), built around a Nikon Ti-E inverted microscope and controlled by the Volocity software (Improvision). Imaging was carried out at 37°C with a 63x PlanApo oil objective (1.45 NA). To prevent unwanted photoactivation of the optogenetic dimerizers, transfected cells were identified with the fluorescence emitted by red fluorescent proteins using a bandpass excitation filter ET 560/30. A 488 nm laser was used to excite EGFP, a 561 nm laser for mCherry and TagRFP-T, and a 640 nm laser for iRFP670. The fluorescence emitted was detected with 527/55nm, 615/70nm and 705/90nm filters, respectively. Whole-cell activation of the photoswitches was achieved by irradiating the field of view with 488 nm laser pulses of 100-200 ms ($3x10^{-3}$ W/cm^2). A built-in photo-perturbation unit was used to deliver 488 nm light (7.07 W/cm^2) pulses with subcellular precision.

Confocal imaging of light-dependent VAPB reconstitution on ER membranes or PH_{OSBP} mediated tethering and light-induced inter-organellar contacts was performed using a customized Nikon Ti-E inverted microscope outfitted with a Yokagowa CSU-X1 spinning disk. Illumination was generated using solid-state laser lines at 488 nm, 561 nm, or 647 nm passed through the pinhole array and into the back aperture of the objective using a quad-pass filter for the appropriate lines (Semrock). Emission light was collected using a 100x Plan-Apochromat 1.49NA oil-immersion objective (Nikon) and focused on a DU-897 EMCCD (Andor) at a final pixel size of 133.3 nm. Specific settings for each color were as follows: 488 – 525/50 emission filter, 50 ms exposure time; 561—605/55 emission filter, 200 ms exposure time; 647—700/75 emission filter, 200 ms exposure time. Cells were imaged in DMEM without phenol red and incubated using a TokaiHit stage-top incubator at 37°C, 5% CO_2.

Image analysis and statistics

Association and dissociation rates for each dimerization system were calculated from changes in prey fluorescence inside a cytosolic ROI before, during, and after the photoactivation and recruitment of the prey protein to mitochondrial membranes. The change in average fluorescence inside the ROI was calculated using the software Fiji (ImageJ Version: 2.0.0-rc-69/1.52p, Wayne Rasband, National

Institute of Health, USA, http://fiji.sc/wiki/index.php/Fiji), and the remainder of the quantification was carried out in MATLAB. The change in fluorescence associated with depletion of the cytosolic pool was calculated as $\frac{\Delta f}{f_\circ} = \frac{f[t_i]-f[t_\circ]}{f[t_\circ]}$, where $f[t] = (F_{\mathrm{ROI}}[t] - F_{\mathrm{bkg}}[t]) \,/\, (F_{\mathrm{cell}}[t] - F_{\mathrm{bkg}}[t])$, where F_{ROI} is the mean fluorescence measured in the cytosolic ROI, F_{bkg} is the mean fluorescence intensity measured in an area of the background, F_{cell} is the mean fluorescence measured in the whole cell to normalize for photobleaching, and t_i denotes the point in time. Changes in iRFP-$PH_{PLC\delta}$ at the plasma membrane in neurons was calculated with the same equation but in this case, the region of interest for each time point was identified by manually drawing an ROI corresponding to the plasma membrane.

The fluorescence changes due to protein recruitment to mitochondria were calculated by measuring the fluorescence signal corresponding to mitochondria at each time point by generating a binary mask using the fluorescence signal associated with the mitochondrial bait. Fluorescence accumulation at mitochondria was measured by dividing the average background-subtracted fluorescence intensity at every time-point (F_t) by the fluorescence intensity of the first time point (F_0) and subsequently normalized to $(Ft - \mathrm{F0})/\mathrm{F0}$.

The relative increase in organelle overlap for each time point upon light-dependent induction of membrane contact sites was performed by generating a binary mask using the fluorescence signal associated with lysosomes in ER-lysosome and mitochondria-lysosome contacts, or with mitochondria in ER-mitochondria contacts. Then the fluorescent signal of the other organelle, corrected for background signal and photobleaching-corrected with the Bleach Correction function in Fiji, was calculated with the following equation $f[t] = (F_{\mathrm{ROI}}[t] - F_{\mathrm{bkg}}[t])$ and normalized to the fluorescence value measured at the beginning of the experiment.

To measure loss of PI4P from the Golgi complex and/or Golgi-endosome-hybrid organelles in experiments involving Opto-VAP, or PH_{OSBP} mediated tethering, in iRFP-P4C expressing HeLa cells, an ROI was drawn around Golgi marker-positive regions. The fluorescence in the ROI at each time point was background-subtracted and photobleaching-corrected using this equation $f[t] = (F_{\mathrm{ROI}}[t] - F_{\mathrm{bkg}}[t]) \,/\, (F_{\mathrm{nucleus}}[t] - F_{\mathrm{bkg}}[t])$. TagRFP-T-$MSP_{VAPB}$-eMagB recruitment to the ER was calculated by measuring the fluorescence signal corresponding to the ER at each time point by generating a binary mask using the fluorescence signal associated with the ER bait acquired during the blue-light stimulation of the optogenetic system. Fluorescence accumulation at the ER was measured dividing the average

fluorescence intensity at every time-point (F_t) background subtracted (F_{bkg}) by the fluorescence intensity of the first time point (F_0) background subtracted according to the formula: $(Ft - \mathrm{Fbkg})/(\mathrm{F0} - \mathrm{Fbkg})$.

Statistical analyses were carried out in GraphPad Prism 8.2.1 (Graph Pad Software).

Kinetics analysis

We found that the apparent kinetics of the Magnets variants reported in this study fit well to an exponential decay model. We used the curve-fitting tool (*cftool*) in MATLAB to determine the kinetic rate constants, τ^{ON} and τ^{OFF}, by fitting the curve to the following equation:

$$S[t] = S_0 + \Delta S\, e^{-\frac{t-t_0}{\tau}}$$

Where $S = \frac{\Delta f}{f_\circ}$, t_0 is time at which the light is turned on or off (for on- or off-kinetics, respectively), S_0 is S at time t_0, and $\Delta S = S_0 - S(\infty)$. During the fitting process, each point is given a weight proportional to $\frac{1}{s.e.m.^2}$. The parameters of the fit can be found in **Supplementary File 6**. For all the datasets acquired in this work, the R^2's obtained for exponential fits are always larger than 0.86 with a median of 0.98.

Acknowledgments: We thank Andrew S. Moore, Benjamin Johnson and Jesse Aaron for discussion and Moritoshi Sato, Tim Levine and Yuxin Mao for providing key reagents. We thank Frank Wilson, Louise Lucast, Heather Wheeler and Alice Dao from the De Camilli lab, and Kevin McGowan, Melissa Ramirez, and Jordan Towne from the Cell and Molecular Biology Shared Resources at Janelia Research Campus for excellent technical support. This work was supported by the NIH (Grants NS36251, P30DK045735 and DA018343) and by the Kavli Foundation to P.D.C., by a fellowship from the Jung Foundation for Science and Research to A.G.S., and by the Howard Hughes Medical Institute. H.F. is a HHMI Life Sciences Associate.

Reagent availability: All eMags constructs have been deposited at Addgene (#162243-162255).

Declaration of interests: The authors declare no competing interests.

SUPPLEMENTARY FILE LEGENDS

Supplementary File 1: Constructs used to express wild-type or mutant Magnets on different subcellular compartments.
The Organelle-Targeting Sequences (OTS) used and their position, the fluorescent tag, and the original or mutant Magnets used in each construct are indicated.

Supplementary File 2: Constructs encoding the soluble prey proteins used in this study.

Supplementary File 3: Mutants tested.

Supplementary File 4: Primers for optimization of the Magnets heterodimer interface.

Supplementary File 5: Primers for thermostabilization of the Magnets proteins.

Supplementary File 6: Fit parameters.

SUPPLEMENTAL INFORMATION

FIGURE SUPPLEMENTS

Figure 1-figure supplement 1

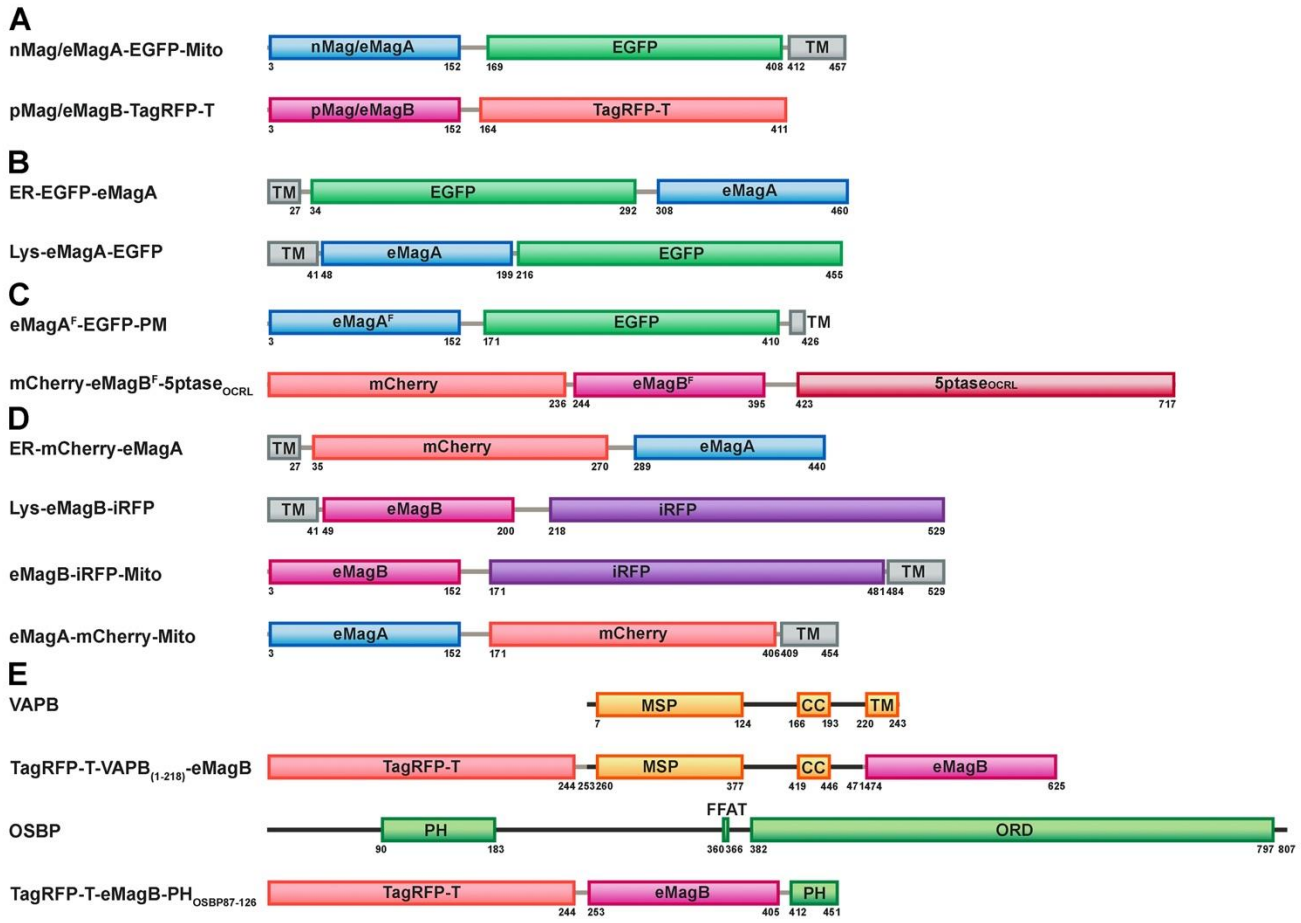

Figure 1-figure supplement 1: Domain organization diagrams of the constructs used in this study.
A. Constructs used to induce wild-type and mutant Magnets heterodimerization at the outer mitochondrial membrane.
B. Bait proteins used for the light-dependent recruitment of soluble prey proteins to the ER and lysosomes.
C. Vectors used for the light-dependent modulation of $PI(4,5)P_2$ at the plasma membrane.
D. Constructs used for the optogenetic induction of organelle contacts.
E. Constructs used to induce VAP reconstitution at the surface at the ER membrane (Opto-VAP). MSP, major sperm protein homology domain; CC, coiled-coil domain; TM, transmembrane domain; PH, Pleckstrin homology domain; FFAT, two phenylalanines (FF) in an Acidic Tract motif; ORD, OSBP-related protein lipid-binding domain.

Figure 1- figure supplement 2

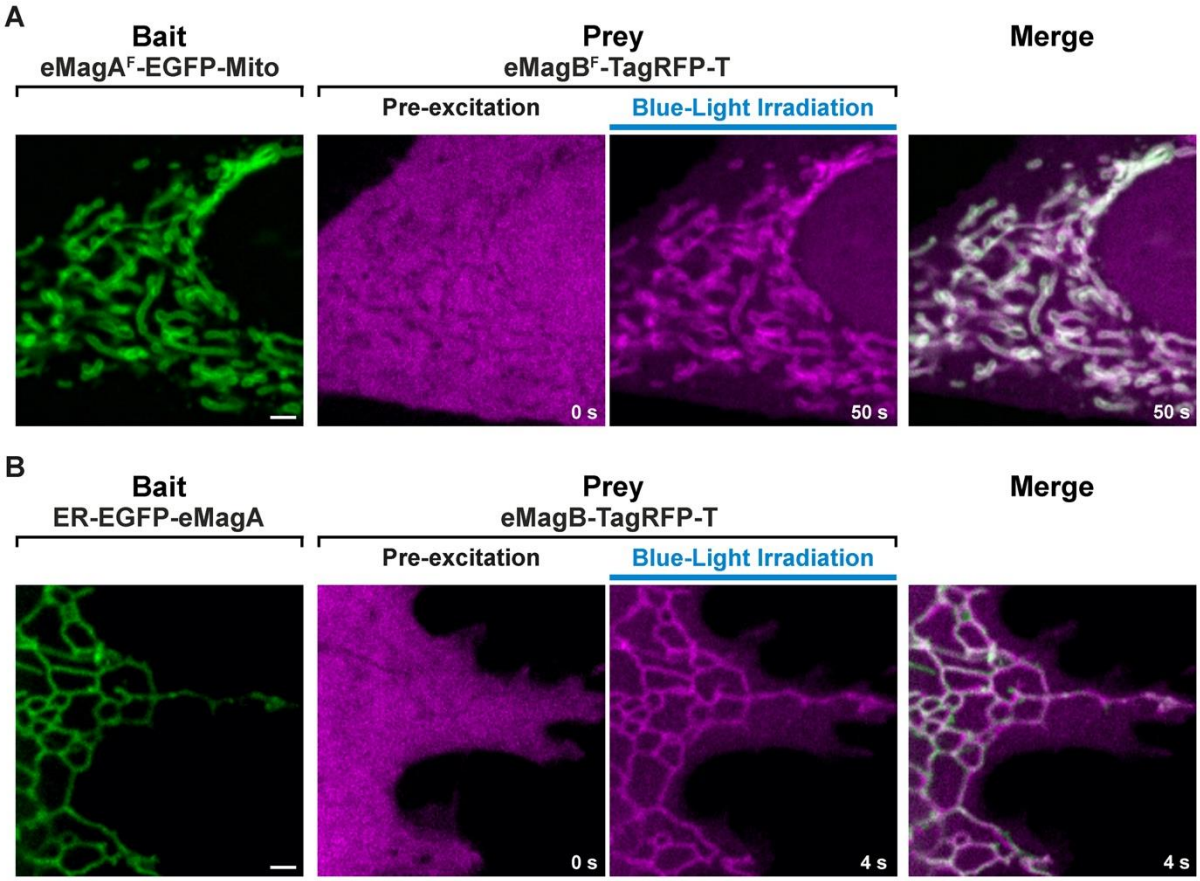

881
882
883 **Figure 1-figure supplement 2: Recruitment of the cytosolic prey to the membrane-associated bait upon light**
884 **stimulation**
885 Accumulation of a soluble prey (eMagB^{F}-TagRFP-T or eMagB-TagRFP-T) to a mitochondria-anchored bait (eMagA^{F}-
886 EGFP-Mito) (A) or to an ER-associated bait (ER-EGFP-eMagA) (B) upon whole-cell illumination in a HeLa cell (A) or
887 COS-7 cell (B). Scale bar: 2 μm.
888
889
890

Figure 1-figure supplement 3

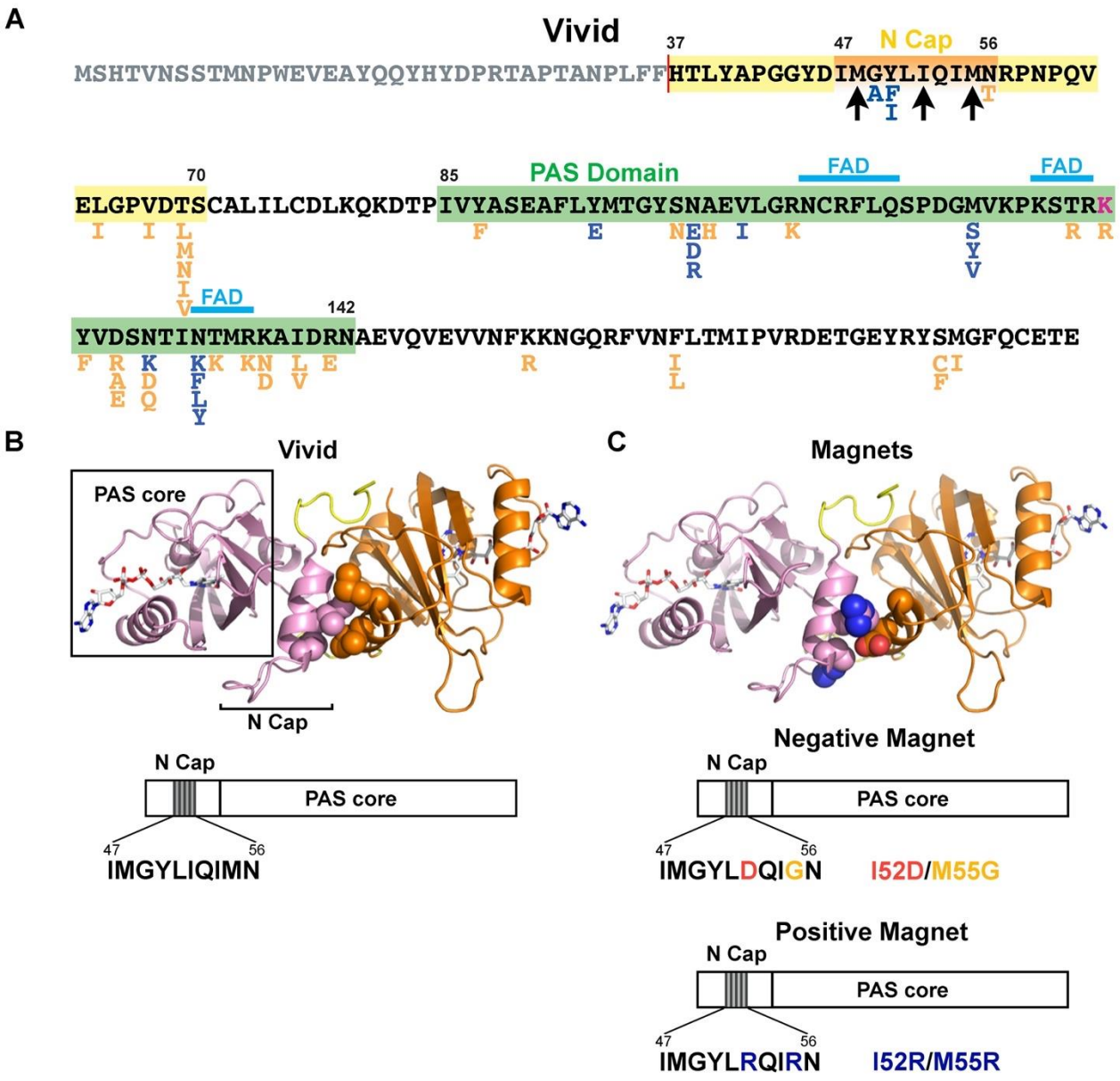

D

Alternative Complementary Charge Tested

nMag	pMag	Result
I52E/M55G	I52R/M55R	Dimerization (-)
I52D/M55A	I52R/M55R	Dimerization (++)
I52D/M55D	I52R/M55R	Dimerization (+)
I52D/M55E	I52R/M55R	No dimerization
I52D/M55G	M48R/I52R/M55R	No dimerization

891

Figure 1-figure supplement 3: Magnets mutations tested to improve heterodimerization efficiency and thermodynamic stability.

A. Primary sequence of the *Neurospora crassa* (strain ATCC 24698) photoreceptor Vivid (UniProtKB Q1K5Y8_NEUCR). The N-cap dimerization domain, the Per-ARNT-Sim (PAS) core domain (the photosensitive portion of the protein), and the amino acids involved in binding the flavin adenine dinucleotide (FAD) cofactor (Heintzen et al., 2001; Zoltowski et al., 2007) are indicated. The construct used for the crystal structure of the homodimer (see below) lacks the N-terminal 36 a.a.; Magnets also lack these 36 a.a. Arrows point to a.a. mutated in an attempt to generate Magnets with improved charge complementarity (see Table in panel D). Amino acid substitutions introduced during the screen are shown below the WT sequence. Magenta: mutations that abolish potential ubiquitination sites; blue, mutations predicted to improve packing or secondary-structure preference; orange, mutations that mimic corresponding residues in thermophilic ascomycetes. The effects on heterodimerization of each substitution and combinations of substitutions is summarized in Supplementary File 3.

B. Crystal structure of the Vivid homodimer and domain cartoon of the monomer. The two monomers are shown in orange and pink. Residues Ile52 and Met55 are shown as spheres.

C. Magnets were generated by introducing mutations to make the interface of one Vivid negatively charged (Ile52Asp/Met55Gly, "negative Magnet"), and the interface of the other Vivid positively charged (Ile52Arg/Met55Arg, "positive Magnets"), so that blue light radiation leads to hetero- rather than homo-dimerization. Residues Asp52/Gly55 in the "negative Magnet" and Arg52/Arg55 of the "positive Magnet" are shown as spheres.

D. Amino acid mutations tested for optimizing charge complementarity. (Scores: (-) less efficient than the original photoreceptors, (+) more efficient, (++) much more efficient).

Figure 1-figure supplement 4

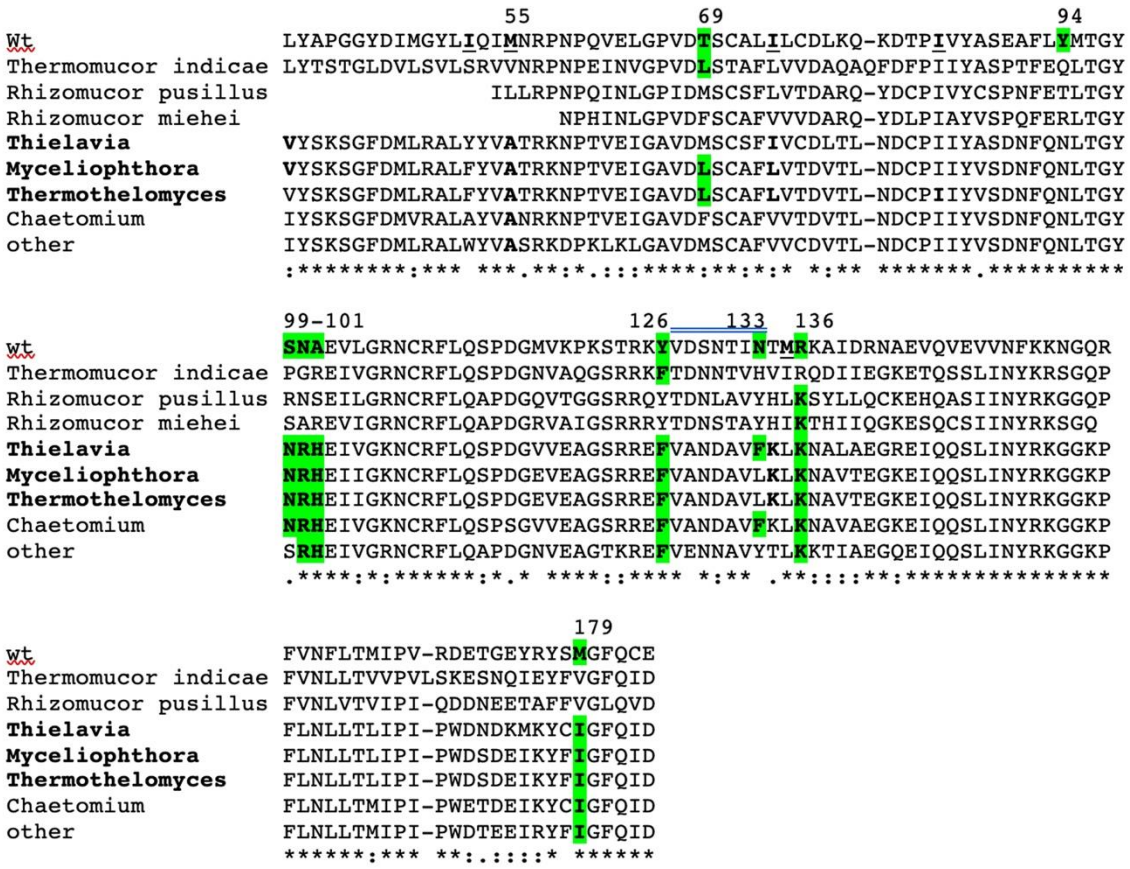

Figure 1-figure supplement 4: Alignment of Vivid domain sequences from thermophilic ascomycetes.
Sequences were retrieved from NCBI. The two *Rhizomucor* sequences come from incomplete whole-genome sequencing projects. The nine mutations in eMags are shown in bold; all but one mutation was to an amino acid occurring in one of the thermophilic homologues. Surprisingly, the 55Ala mutation introduced by rational design was subsequently found to occur at that position in many thermophilic homologues.

Figure 1-figure supplement 5

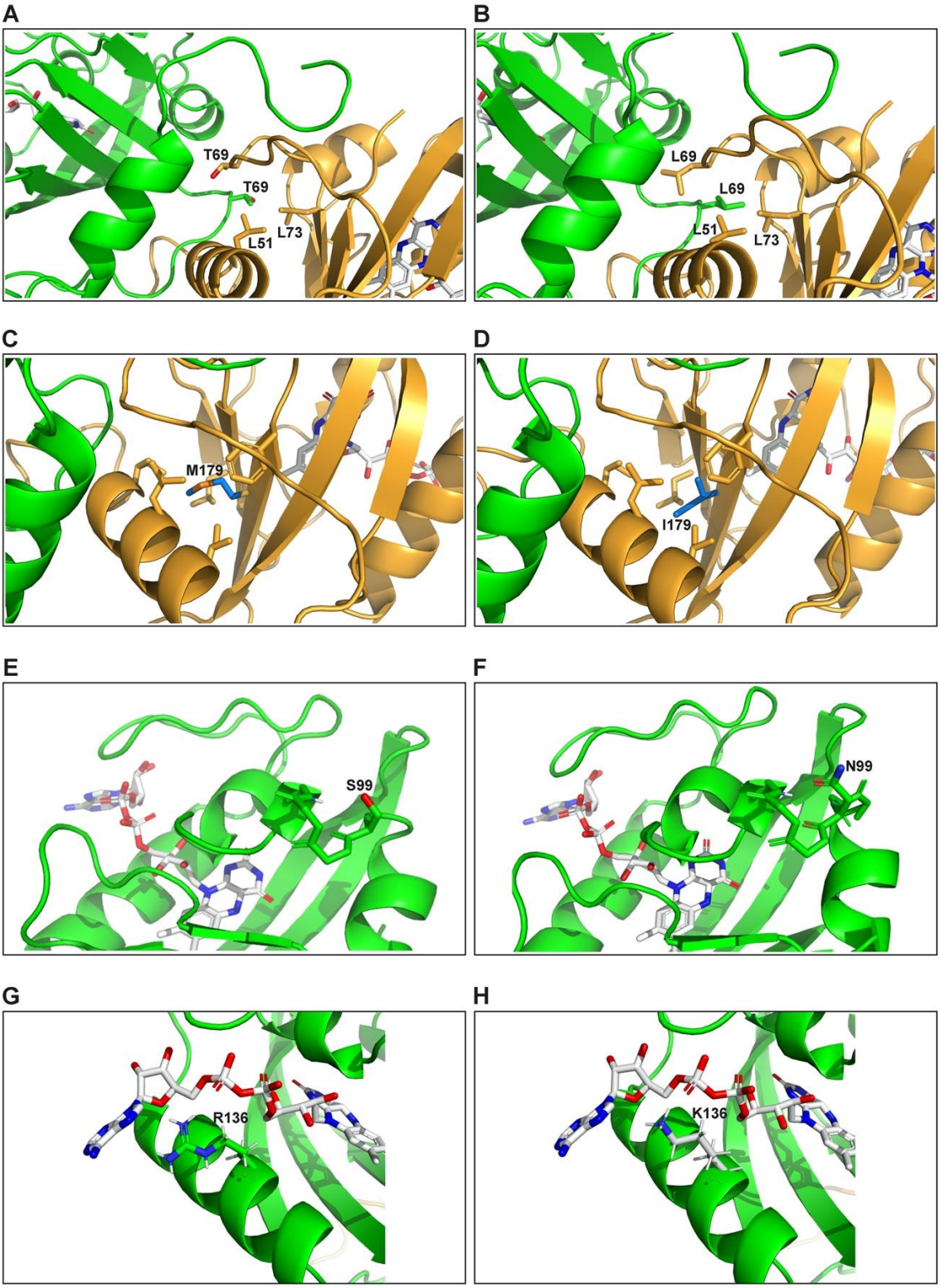

947

948

Figure 1-figure supplement 5: Molecular modeling of effects of specific eMags mutations.
A. Wild-type Thr69 leaves an unsatisfied hydrogen bond donor and acceptor at the dimer interface and packs poorly. Thr also prefers strand over helix (this position is in a helical turn).
B. Thr69Leu shows much greater hydrophobic packing at the dimer interface, including with Leu69 on the other dimer half. Leu also prefers helix over strand.
C. Wild-type Met179 is a sub-standard hydrophobic packer and has high residue entropy. Met also has only modest preference for strand over helix.
D. Met179Ile makes more hydrophobic contacts and has low residue entropy. Ile also has excellent preference for strand over helix.
E. Wild-type Ser99 makes a weak "helix N-cap" hydrogen bond to the backbone amide H of residue 102. Ser is also only weakly preferred as a residue in a helix N-cap turn.
F. Ser99Asn makes a strong "helix N-cap" hydrogen bond to the backbone amide H of residue 102. Asn is also by far the most strongly preferred residue in a helix N-cap turn.
G. Wild-type Arg136 makes an ion pair with a phosphate of FAD, but quite closely approaches the adenine ring, with which it has suboptimal packing and electrostatics.
H. Arg136Lys still makes the ion pair with a phosphate of FAD, and less closely approaches the adenine ring, decreasing unfavorable contacts.

Figure 1-figure supplement 6

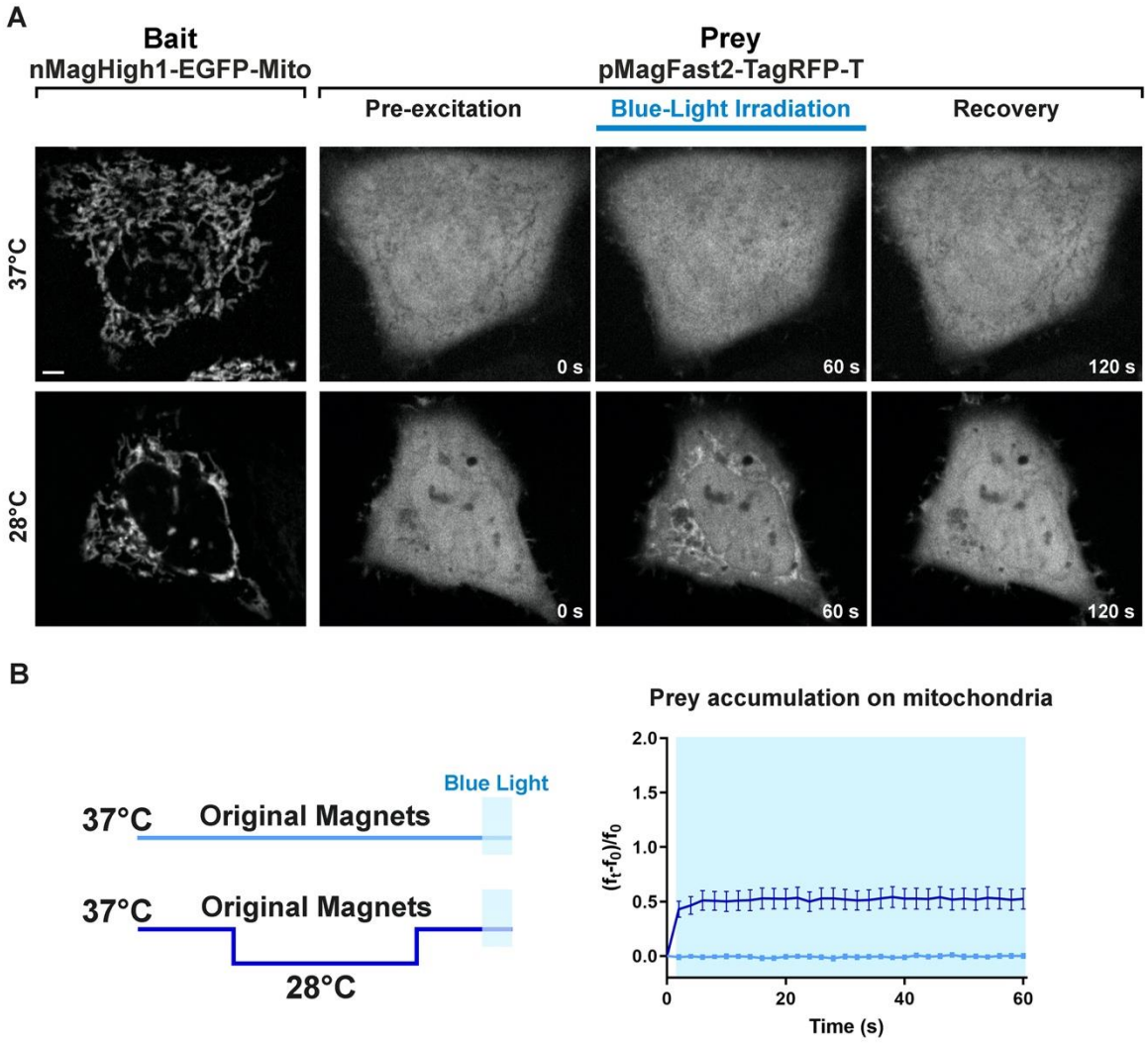

Figure 1-figure supplement 6: Light-dependent heterodimerization of the original Magnets at the mitochondrial surface with or without preincubation of cells at 28°C.

A. Representative example of the light-dependent recruitment of the original Magnets prey (pMagFast2-TagRFP-T) to mitochondria in HeLa cells expressing the mitochondrial bait nMagHigh1-EGFP-Mito without (top) or with (bottom) a preincubation at 28°C. Scale bar: 5 μm.

B. Plot showing the accumulation of soluble prey from the cytosol to mitochondria in cells expressing the original Magnets either without or with a preincubation at 28°C for 12-24 hours prior to imaging and irradiation, as shown in the schematic at left (N = original Magnets: 12 cells, original Magnets (28°C): 17 cells; from 3 independent experiments).

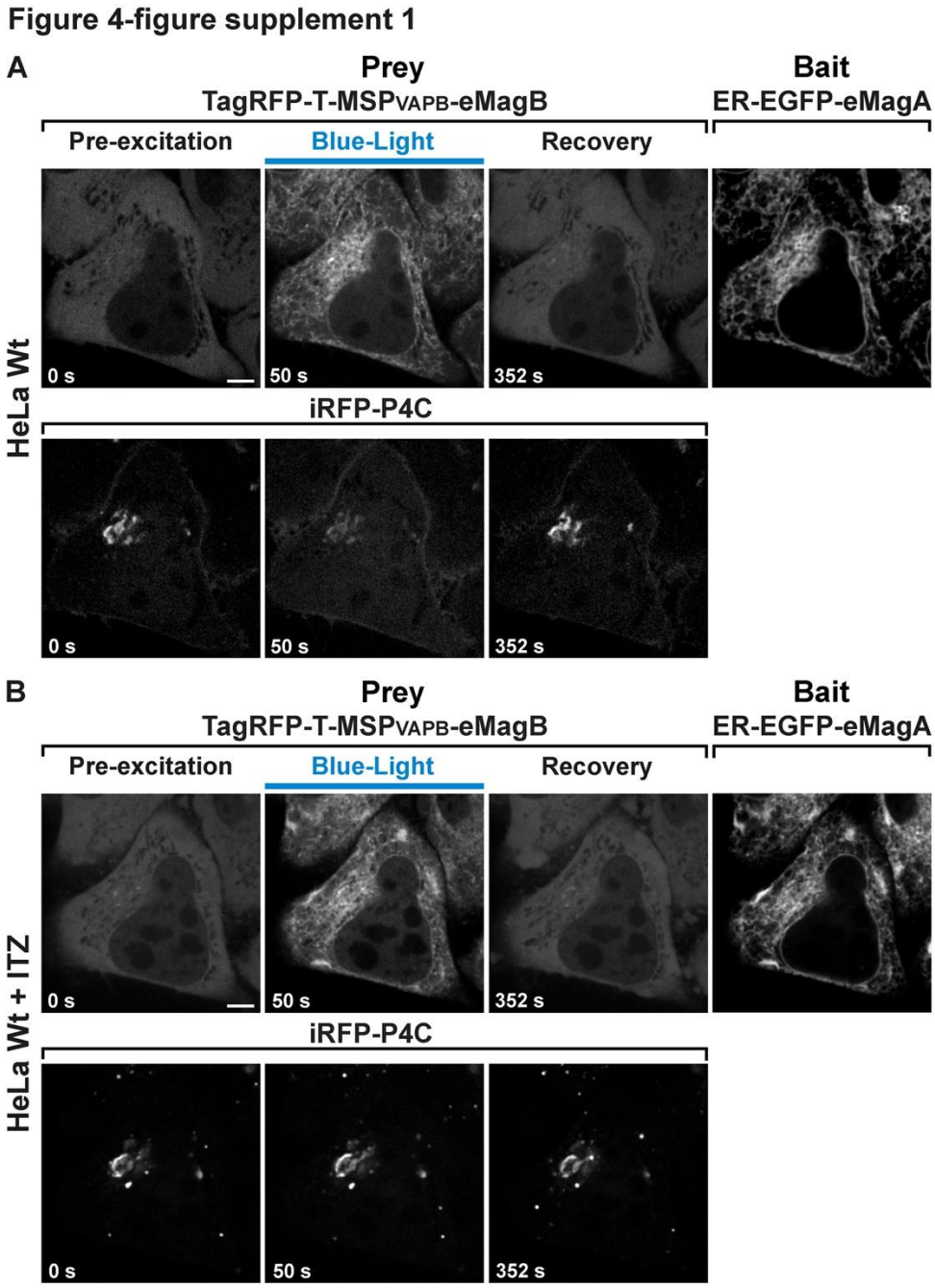

Figure 4-figure supplement 1: Opto-VAP reconstitution induces PI4P loss from the Golgi complex and this effect is blocked by ITZ treatment.

The same wild-type HeLa cell expressing TagRFP-T-MSP($VAPB_{(1-218)}$)-eMagB, ER-EGFP-eMagA and the PI4P reporter iRFP-P4C was imaged before (A) and 45 min after ITZ treatment (B). Before ITZ treatment, we could detect a reduction in iRFP-P4C (PI4P) from the Golgi upon illumination (panel A, lower row). However, after ITZ incubation, we could not visualize iRFP-P4C loss upon illumination despite efficient activation of Opto-VAP (panel B, lower row). Scale bar: 5 µm.

Figure 4-figure supplement 2

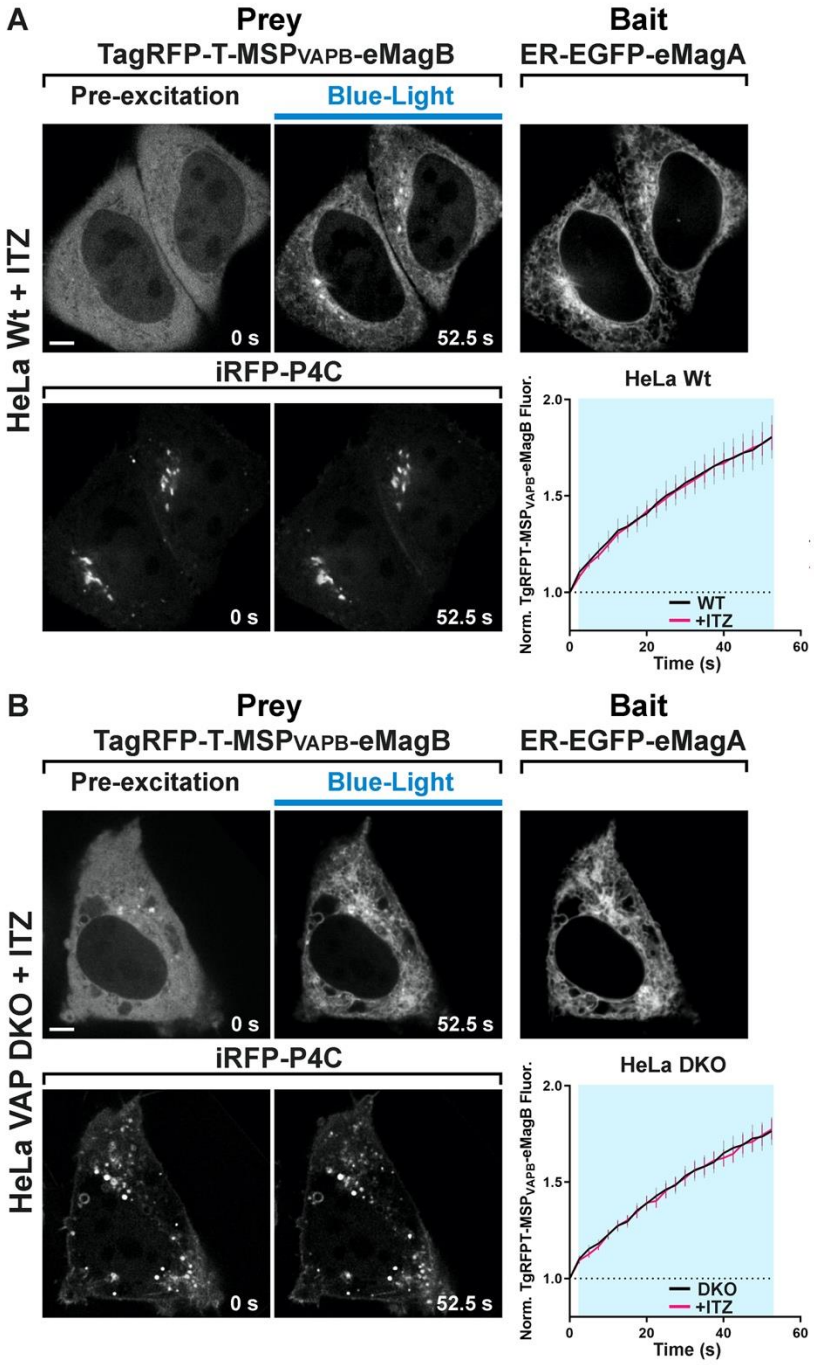

Figure 4-figure supplement 2: ITZ treatment blocks PI4P loss from the Golgi complex but does not affect Opto-VAP reconstitution in WT and VAP DKO HeLa cells.

Wild-type (A) and VAP-DKO (B) HeLa cells expressing TagRFP-T-MSP($VAPB_{(1-218)}$)-eMagB, ER-EGFP-eMagA and the PI4P reporter iRFP-P4C imaged 30 min after ITZ treatment. Despite the rapid and efficient association of TagRFP-T-MSP($VAPB_{(1-218)}$)-eMagB to ER membranes upon light stimulation (graphs at right), ITZ prevented iRFP-P4C (PI4P) loss from the Golgi in wild-type HeLa cells and endosome/Golgi hybrid structures in HeLa VAP-DKO cells. Scale bar: 5 µm. (HeLa WT: τ^{ON} = 50.7 ± 3.2 s, N=24; HeLa WT + ITZ: τ^{ON} = 46.5 ± 2.7 s, N=16; HeLa VAP-DKO: τ^{ON} = 81.1 ± 9.6 s, N=20; HeLa VAP-DKO + ITZ: τ^{ON} = 68.1 ± 8.2 s, N=16; from 3 independent experiments).

Figure 4-figure supplement 3

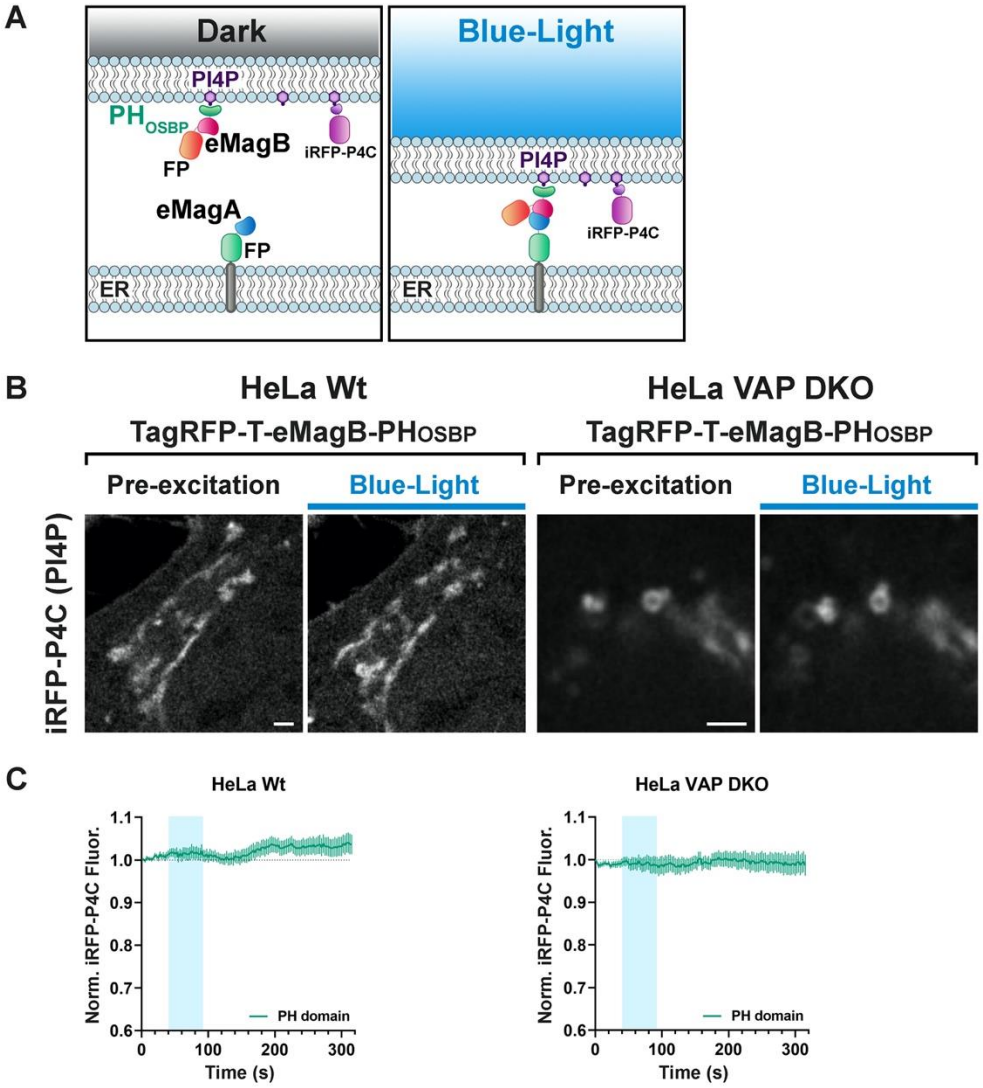

Figure 4-figure supplement 3: PH_{OSBP} mediated tethering between the ER and PI4P-rich subcellular membranes is not associated with PI4P loss from these membranes

A. Graphical representation of the assay used to mediate VAP-independent membrane tethering of PI4P-enriched Golgi and endosomal membranes to the ER. Cells were transfected with 1) the PH domain of OSBP fused to TagRFP-T and eMagB (TagRFP-T-eMagB-PH_{OSBP}), 2) an ER bait (ER-EGFP-eMagA), and 3) a PI4P reporter (iRFP-P4C). Before light activation (Dark), TagRFP-T-eMagB-PH_{OSBP} is partially cytosolic and already partially bound to PI4P-enriched Golgi membranes (in WT cells) and Golgi/endosome hybrid membranes (in VAP-DKO cells). Upon blue-light illumination, eMags associated with the ER, including ER in proximity of the Golgi and endosomes, brings PI4P-enriched Golgi, or hybrid endosome-Golgi organelles, in close apposition to the ER, but no PI4P loss occurs given the absence of the ORD.

B. High-magnification view of the Golgi complex of a WT cell and of the hybrid Golgi/endosome organelles of a VAP-DKO HeLa cell expressing the constructs indicated in (A). The iRFP-P4C (PI4P) signal is shown. Blue light-dependent formation of the tether does not reduce PI4P levels on these organelles. Scale bar: 5 µm (WT) and 2 µm (DKO).

C. Quantification of the results shown in (B). WT HeLa (N= 16); VAP-DKO HeLa (N= 17).

VIDEO LEGENDS

Video 1: Rapid and reversible recruitment of the cytosolic prey eMagB-TagRFP-T to the mitochondrially associated bait eMagA-EGFP-Mito (Hela cells). Whole-cell illumination with 0.5 Hz blue-light pulses for 60 s. Scale bar: 5 μm.

Video 2: Rapid and reversible accumulation of the cytosolic prey eMagB-TagRFP-T on the surface of the endoplasmic reticulum in COS7 cells expressing the ER-associated bait ER-EGFP-eMagA. Whole-cell illumination experiment. Scale bar: 2 μm.

Video 3: Localized recruitment of the cytosolic prey eMagB-TagRFP-T to the ER-associated bait ER-EGFP-eMagA in a 3 μm x 3 μm ROI (blue square) of the ER. HeLa cell. Scale bar: 5 μm.

Video 4: Soluble prey (eMagB-TagRFP-T) recruitment to individual lysosomes identified by the lysosomal marker Lamp1-iRFP, in primary hippocampal neurons at 14 DIVs, expressing the lysosome-specific bait Lys-eMagA-EGFP. Scale bar: 5 μm.

Video 5: Rapid cycles of $PI(4,5)P_2$ dephosphorylation and rephosphorylation in primary hippocampal neurons at 7 DIV. Scale bar: 5 μm.

Video 6: Light-induced contacts between the ER and lysosomes in COS7 cells expressing ER-mCherry-eMagA (green) and Lys-eMagB-iRFP (magenta). Scale bar: 2 μm.

Video 7: Light-induced contacts between the ER and mitochondria in HeLa cells expressing ER-mCherry-eMagA (green) and eMagB-iRFP-Mito (magenta). Scale bar: 2 μm.

Video 8: Light-induced contacts between mitochondria and lysosomes in HeLa cells expressing eMagA-mCherry-Mito (green) and Lys-eMagB-iRFP (magenta). Scale bar: 2 μm.

Video 9: Fission of a mitochondrion caused by a moving lysosome anchored to the mitochondrion upon light-dependent interaction mediated by eMag dimerization. HeLa cells expressing eMagA-mCherry-Mito (green) and Lys-eMagB-iRFP (magenta). Scale bar: 0.5 μm.

Video 10: Rapid and reversible loss of iRFP-P4C from the Golgi upon light-dependent reconstitution of VAPB on ER membranes in wild-type HeLa cells. TagRFP-T-$VAPB_{(1-218)}$-eMagB is shown on the left, iRFP-P4C is shown on the right. Scale bar: 5 μm.

Video 11: Rapid and reversible loss of iRFP-P4C from Golgi/endosome hybrid organelles in VAP-DKO HeLa cells upon light-dependent reconstitution of VAPB on ER membranes. TagRFP-T-$VAPB_{(1-218)}$-eMagB is shown on the left, iRFP-P4C is shown on the right. Scale bar: 5 μm.

REFERENCES

Benedetti L, Barentine AES, Messa M, Wheeler H, Bewersdorf J, Camilli PD. 2018. Light-activated protein interaction with high spatial subcellular confinement. *Proc National Acad Sci* **115**:E2238–E2245. doi:10.1073/pnas.1713845115

Bergeijk P van, Adrian M, Hoogenraad CC, Kapitein LC. 2015. Optogenetic control of organelle transport and positioning. *Nature* **518**:111–114. doi:10.1038/nature14128

Bracha D, Walls MT, Wei M-T, Zhu L, Kurian M, Avalos JL, Toettcher JE, Brangwynne CP. 2018. Mapping Local and Global Liquid Phase Behavior in Living Cells Using Photo-Oligomerizable Seeds. *Cell* **175**:1467-1480.e13. doi:10.1016/j.cell.2018.10.048

Bugaj LJ, Choksi AT, Mesuda CK, Kane RS, Schaffer DV. 2013. Optogenetic protein clustering and signaling activation in mammalian cells. *Nat Methods* **10**:249–252. doi:10.1038/nmeth.2360

Che DL, Duan L, Zhang K, Cui B. 2015. The Dual Characteristics of Light-Induced Cryptochrome 2, Homo-oligomerization and Heterodimerization, for Optogenetic Manipulation in Mammalian Cells. *Acs Synth Biol* **4**:1124–35. doi:10.1021/acssynbio.5b00048

Choy E, Chiu VK, Silletti J, Feoktistov M, Morimoto T, Michaelson D, Ivanov IE, Philips MR. 1999. Endomembrane Trafficking of Ras. *Cell* **98**:69–80. doi:10.1016/s0092-8674(00)80607-8

DeRose R, Miyamoto T, Inoue T. 2013. Manipulating signaling at will: chemically-inducible dimerization (CID) techniques resolve problems in cell biology. *Pflügers Archiv European J Physiology* **465**:409–17. doi:10.1007/s00424-012-1208-6

Dine E, Gil AA, Uribe G, Brangwynne CP, Toettcher JE. 2018. Protein Phase Separation Provides Long-Term Memory of Transient Spatial Stimuli. *Cell Syst* **6**:655-663.e5. doi:10.1016/j.cels.2018.05.002

Dong R, Saheki Y, Swarup S, Lucast L, Harper JW, Camilli PD. 2016. Endosome-ER Contacts Control Actin Nucleation and Retromer Function through VAP-Dependent Regulation of PI4P. *Cell* **166**:408–23. doi:10.1016/j.cell.2016.06.037

Duan L, Che D, Zhang K, Ong Q, Guo S, Cui B. 2015. Optogenetic control of molecular motors and organelle distributions in cells. *Chem Biol* **22**:671–82. doi:10.1016/j.chembiol.2015.04.014

Duan L, Hope J, Ong Q, Lou H-Y, Kim N, McCarthy C, Acero V, Lin MZ, Cui B. 2017. Understanding CRY2 interactions for optical control of intracellular signaling. *Nat Commun* **8**:547. doi:10.1038/s41467-017-00648-8

Furuya A, Kawano F, Nakajima T, Ueda Y, Sato M. 2017. Assembly Domain-Based Optogenetic System for the Efficient Control of Cellular Signaling. *Acs Synth Biol* **6**:1086–1095. doi:10.1021/acssynbio.7b00022

Gasser C, Taiber S, Yeh C-M, Wittig CH, Hegemann P, Ryu S, Wunder F, Möglich A. 2014. Engineering of a red-light-activated human cAMP/cGMP-specific phosphodiesterase. *P Natl Acad Sci Usa* **111**:8803–8. doi:10.1073/pnas.1321600111

Gray NW, Weimer RM, Bureau I, Svoboda K. 2006. Rapid Redistribution of Synaptic PSD-95 in the Neocortex In Vivo. *Plos Biol* **4**:e370. doi:10.1371/journal.pbio.0040370

Grusch M, Schelch K, Riedler R, Reichhart E, Differ C, Berger W, Inglés-Prieto Á, Janovjak H. 2014. Spatio-temporally precise activation of engineered receptor tyrosine kinases by light. *Embo J* **33**:1713–26. doi:10.15252/embj.201387695

Guglielmi G, Barry JD, Huber W, De Renzis S. 2015. An Optogenetic Method to Modulate Cell Contractility during Tissue Morphogenesis. *Dev Cell* **35**:646–660. doi:10.1016/j.devcel.2015.10.020

Guntas G, Hallett RA, Zimmerman SP, Williams T, Yumerefendi H, Bear JE, Kuhlman B. 2014. Engineering an improved light-induced dimer (iLID) for controlling the localization and activity of signaling proteins. *P Natl Acad Sci Usa* **112**:112–7. doi:10.1073/pnas.1417910112

Hallett RA, Zimmerman SP, Yumerefendi H, Bear JE, Kuhlman B. 2015. Correlating in Vitro and in Vivo Activities of Light-Inducible Dimers: A Cellular Optogenetics Guide. *Acs Synth Biol* **5**:53–64. doi:10.1021/acssynbio.5b00119

Hammond GRV, Balla T. 2015. Polyphosphoinositide binding domains: Key to inositol lipid biology. *Biochim Biophys Acta* **1851**:746–58. doi:10.1016/j.bbalip.2015.02.013

Haren J van, Charafeddine RA, Ettinger A, Wang H, Hahn KM, Wittmann T. 2018. Local control of intracellular microtubule dynamics by EB1 photodissociation. *Nat Cell Biol* **20**:252–261. doi:10.1038/s41556-017-0028-5

Heintzen C, Loros JJ, Dunlap JC. 2001. The PAS Protein VIVID Defines a Clock-Associated Feedback Loop that Represses Light Input, Modulates Gating, and Regulates Clock Resetting. *Cell* **104**:453–464. doi:10.1016/s0092-8674(01)00232-x

Idevall-Hagren O, Dickson EJ, Hille B, Toomre DK, Camilli PD. 2012. Optogenetic control of phosphoinositide metabolism. *P Natl Acad Sci Usa* **109**:E2316-23. doi:10.1073/pnas.1211305109

Kaberniuk AA, Shemetov AA, Verkhusha VV. 2016. A bacterial phytochrome-based optogenetic system controllable with near-infrared light. *Nat Methods* **13**:591–7. doi:10.1038/nmeth.3864

Kaiser SE, Brickner JH, Reilein AR, Fenn TD, Walter P, Brunger AT. 2005. Structural Basis of FFAT Motif-Mediated ER Targeting. *Structure* **13**:1035–1045. doi:10.1016/j.str.2005.04.010

Kawano F, Okazaki R, Yazawa M, Sato M. 2016. A photoactivatable Cre–loxP recombination system for optogenetic genome engineering. *Nat Chem Biol* **12**:1059–1064. doi:10.1038/nchembio.2205

1137 Kawano F, Suzuki H, Furuya A, Sato M. 2015. Engineered pairs of distinct photoswitches for
1138 optogenetic control of cellular proteins. *Nat Commun* **6**:6256. doi:10.1038/ncomms7256

1139 Kennedy MJ, Hughes RM, Peteya LA, Schwartz JW, Ehlers MD, Tucker CL. 2010. Rapid blue-light-
1140 mediated induction of protein interactions in living cells. *Nat Methods* **7**:973–5.
1141 doi:10.1038/nmeth.1524

1142 Kim S, Leal SS, Halevy DB, Gomes CM, Lev S. 2010. Structural requirements for VAP-B
1143 oligomerization and their implication in amyotrophic lateral sclerosis-associated VAP-B(P56S)
1144 neurotoxicity. *J Biological Chem* **285**:13839–49. doi:10.1074/jbc.m109.097345

1145 Lerner A, Yumerefendi H, Goudy O, Strahl BD, Kuhlman B. 2018. Engineering Improved
1146 Photoswitches for the Control of Nucleocytoplasmic Distribution. *Acs Synth Biol* **7**:2898–2907.
1147 doi:10.1021/acssynbio.8b00368

1148 Levskaya A, Weiner OD, Lim WA, Voigt CA. 2009. Spatiotemporal control of cell signalling using a
1149 light-switchable protein interaction. *Nature* **461**:997–1001. doi:10.1038/nature08446

1150 Losi A, Gardner KH, Möglich A. 2018. Blue-Light Receptors for Optogenetics. *Chem Rev* **118**:10659–
1151 10709. doi:10.1021/acs.chemrev.8b00163

1152 Lungu OI, Hallett RA, Choi EJ, Aiken MJ, Hahn KM, Kuhlman B. 2012. Designing photoswitchable
1153 peptides using the AsLOV2 domain. *Chem Biol* **19**:507–17. doi:10.1016/j.chembiol.2012.02.006

1154 Luo X, Wasilko DJ, Liu Y, Sun J, Wu X, Luo Z-Q, Mao Y. 2015. Structure of the Legionella Virulence
1155 Factor, SidC Reveals a Unique PI(4)P-Specific Binding Domain Essential for Its Targeting to the
1156 Bacterial Phagosome. *Plos Pathog* **11**:e1004965. doi:10.1371/journal.ppat.1004965

1157 Mesmin B, Bigay J, Moser von Filseck J, Lacas-Gervais S, Drin G, Antonny B. 2013. A Four-Step
1158 Cycle Driven by PI(4)P Hydrolysis Directs Sterol/PI(4)P Exchange by the ER-Golgi Tether OSBP.
1159 *Cell* **155**:830–843. doi:10.1016/j.cell.2013.09.056

1160 Murphy SE, Levine TP. 2016. VAP, a Versatile Access Point for the Endoplasmic Reticulum: Review
1161 and analysis of FFAT-like motifs in the VAPome. *Biochim Biophys Acta* **1861**:952–61.
1162 doi:10.1016/j.bbalip.2016.02.009

1163 Nada S, Mori S, Takahashi Y, Okada M. 2014. Methods in Enzymology. *Methods Enzymol* **535**:249–
1164 263. doi:10.1016/b978-0-12-397925-4.00015-8

1165 Nehls S, Snapp EL, Cole NB, Zaal KJM, Kenworthy AK, Roberts TH, Ellenberg J, Presley JF, Siggia E,
1166 Lippincott-Schwartz J. 2000. Dynamics and retention of misfolded proteins in native ER membranes.
1167 *Nat Cell Biol* **2**:288–295. doi:10.1038/35010558

1168 Nemoto Y, Camilli PD. 1999. Recruitment of an alternatively spliced form of synaptojanin 2 to
1169 mitochondria by the interaction with the PDZ domain of a mitochondrial outer membrane protein.
1170 *Embo J* **18**:2991–3006. doi:10.1093/emboj/18.11.2991

1171 Nijenhuis W, Grinsven MMP van, Kapitein LC. 2020. An optimized toolbox for the optogenetic control
1172 of intracellular transport. *J Cell Biology* **219**. doi:10.1083/jcb.201907149

1173 Niopek D, Benzinger D, Roensch J, Draebing T, Wehler P, Eils R, Ventura BD. 2014. Engineering
1174 light-inducible nuclear localization signals for precise spatiotemporal control of protein dynamics in
1175 living cells. *Nat Commun* **5**:4404. doi:10.1038/ncomms5404

1176 Niopek D, Wehler P, Roensch J, Eils R, Ventura BD. 2016. Optogenetic control of nuclear protein
1177 export. *Nat Commun* **7**:10624. doi:10.1038/ncomms10624

1178 Oliveira TB de, Rodrigues A. 2019. Fungi in Extreme Environments: Ecological Role and
1179 Biotechnological Significance 39–57. doi:10.1007/978-3-030-19030-9_3

1180 Pathak GP, Strickland D, Vrana JD, Tucker CL. 2014. Benchmarking of Optical Dimerizer Systems. *Acs*
1181 *Synth Biol* **3**:832–838. doi:10.1021/sb500291r

1182 Pirruccello M, Camilli PD. 2012. Inositol 5-phosphatases: insights from the Lowe syndrome protein
1183 OCRL. *Trends Biochem Sci* **37**:134–43. doi:10.1016/j.tibs.2012.01.002

1184 Putyrski M, Schultz C. 2012. Protein translocation as a tool: The current rapamycin story. *Febs Lett*
1185 **586**:2097–105. doi:10.1016/j.febslet.2012.04.061

1186 Rost BR, Schneider-Warme F, Schmitz D, Hegemann P. 2017. Optogenetic Tools for Subcellular
1187 Applications in Neuroscience. *Neuron* **96**:572–603. doi:10.1016/j.neuron.2017.09.047

1188 Saint-Jean M de, Delfosse V, Douguet D, Chicanne G, Payrastre B, Bourguet W, Antonny B, Drin G.
1189 2011. Osh4p exchanges sterols for phosphatidylinositol 4-phosphate between lipid bilayers. *J Cell*
1190 *Biology* **195**:965–78. doi:10.1083/jcb.201104062

1191 Shaner NC, Lin MZ, McKeown MR, Steinbach PA, Hazelwood KL, Davidson MW, Tsien RY. 2008.
1192 Improving the photostability of bright monomeric orange and red fluorescent proteins. *Nat Methods*
1193 **5**:545–51. doi:10.1038/nmeth.1209

1194 Shcherbakova DM, Verkhusha VV. 2013. Near-infrared fluorescent proteins for multicolor in vivo
1195 imaging. *Nat Methods* **10**:751–4. doi:10.1038/nmeth.2521

1196 Shin Y, Berry J, Pannucci N, Haataja MP, Toettcher JE, Brangwynne CP. 2017. Spatiotemporal Control
1197 of Intracellular Phase Transitions Using Light-Activated optoDroplets. *Cell* **168**:159-171.e14.
1198 doi:10.1016/j.cell.2016.11.054

1199 Spencer DM, Wandless TJ, Schreiber SL, Crabtree GR. 1993. Controlling signal transduction with
1200 synthetic ligands. *Sci New York N Y* **262**:1019–24. doi:10.1126/science.7694365

1201 Strating JRPM, Linden L van der, Albulescu L, Bigay J, Arita M, Delang L, Leyssen P, Schaar HM van
1202 der, Lanke KHW, Thibaut HJ, Ulferts R, Drin G, Schlinck N, Wubbolts RW, Sever N, Head SA, Liu
1203 JO, Beachy PA, Matteis MAD, Shair MD, Olkkonen VM, Neyts J, Kuppeveld FJM van. 2015.

Itraconazole inhibits enterovirus replication by targeting the oxysterol-binding protein. *Cell Reports* **10**:600–15. doi:10.1016/j.celrep.2014.12.054

Strickland D, Lin Y, Wagner E, Hope CM, Zayner J, Antoniou C, Sosnick TR, Weiss EL, Glotzer M. 2012. TULIPs: tunable, light-controlled interacting protein tags for cell biology. *Nat Methods* **9**:379–84. doi:10.1038/nmeth.1904

Szczesna-Skorupa E, Kemper B. 2000. Endoplasmic Reticulum Retention Determinants in the Transmembrane and Linker Domains of Cytochrome P450 2C1. *J Biol Chem* **275**:19409–19415. doi:10.1074/jbc.m002394200

Taslimi A, Zoltowski B, Miranda JG, Pathak GP, Hughes RM, Tucker CL. 2016. Optimized second-generation CRY2-CIB dimerizers and photoactivatable Cre recombinase. *Nat Chem Biol* **12**:425–30. doi:10.1038/nchembio.2063

Toettcher JE, Gong D, Lim WA, Weiner OD. 2011. Light-based feedback for controlling intracellular signaling dynamics. *Nat Methods* **8**:837–9. doi:10.1038/nmeth.1700

Toettcher JE, Weiner OD, Lim WA. 2013. Using optogenetics to interrogate the dynamic control of signal transmission by the Ras/Erk module. *Cell* **155**:1422–34. doi:10.1016/j.cell.2013.11.004

Vaidya AT, Chen C-H, Dunlap JC, Loros JJ, Crane BR. 2011. Structure of a light-activated LOV protein dimer that regulates transcription. *Sci Signal* **4**:ra50. doi:10.1126/scisignal.2001945

Venditti R, Rega LR, Masone MC, Santoro M, Polishchuk E, Sarnataro D, Paladino S, D'Auria S, Varriale A, Olkkonen VM, Tullio GD, Polishchuk R, Matteis MAD. 2019. Molecular determinants of ER–Golgi contacts identified through a new FRET–FLIM system. *J Cell Biol* **218**:1055–1065. doi:10.1083/jcb.201812020

Wong YC, Ysselstein D, Krainc D. 2018. Mitochondria–lysosome contacts regulate mitochondrial fission via RAB7 GTP hydrolysis. *Nature* **554**:382–386. doi:10.1038/nature25486

Wu YI, Frey D, Lungu OI, Jaehrig A, Schlichting I, Kuhlman B, Hahn KM. 2009. A genetically encoded photoactivatable Rac controls the motility of living cells. *Nature* **461**:104–8. doi:10.1038/nature08241

Yazawa M, Sadaghiani AM, Hsueh B, Dolmetsch RE. 2009. Induction of protein-protein interactions in live cells using light. *Nat Biotechnol* **27**:941–945. doi:10.1038/nbt.1569

Zewe JP, Wills RC, Sangappa S, Goulden BD, Hammond GR. 2018. SAC1 degrades its lipid substrate PtdIns4P in the endoplasmic reticulum to maintain a steep chemical gradient with donor membranes. *Elife* **7**:e35588. doi:10.7554/elife.35588

Zimmerman SP, Hallett RA, Bourke AM, Bear JE, Kennedy MJ, Kuhlman B. 2016. Tuning the Binding Affinities and Reversion Kinetics of a Light Inducible Dimer Allows Control of Transmembrane Protein Localization. *Biochemistry-us* **55**:5264–71. doi:10.1021/acs.biochem.6b00529

Zoltowski BD, Schwerdtfeger C, Widom J, Loros JJ, Bilwes AM, Dunlap JC, Crane BR. 2007. Conformational Switching in the Fungal Light Sensor Vivid. *Science* **316**:1054–1057. doi:10.1126/science.1137128

Zoltowski BD, Vaccaro B, Crane BR. 2009. Mechanism-based tuning of a LOV domain photoreceptor. *Nat Chem Biol* **5**:827–34. doi:10.1038/nchembio.210

Key Resources Table

Key Resources Table				
Reagent type (species) or resource	**Designation**	**Source or reference**	**Identifiers**	**Additional information**
Sequence-based reagent	eMagA^{F} ATGGGACACACT CTTTACGCCCCT GGAGGATACGAC ATTATGGGATAT TTGGATCAGATT GCGAACCGCCCA AACCCTCAGGTC GAACTGGGGCCT GTGGACCTGTCA TGTGCCCTGATC CTGTGCGATCTG AAGCAAAAGGAC ACTCCGATCGTC TACGCCTCGGAA GCCTTCTTGGAG ATGACCGGATAC AACAGACATGAG GTGCTCGGCAGG AACTGCAGATTC CTGCAGTCCCCC GACGGGATGGTG AAACCAAAGTCG ACTCGCAAATAT GTGGACTCGAAC ACGATCTTCACC ATCAAGAAGGCC ATCGACCGGAAC GCCGAGGTCCAG GTGGAGGTGGTC AACTTTAAGAAG AACGGCCAGCGG TTCGTGAACTTT CTGACCATCATT CCGGTCCGGGAT GAAACCGGAGAG TACAGATACTCC ATCGGATTCCAG TGCGAAACCGAA	This paper	GenBank accession number: MW203024	See Main Text, Materials and Methods and Supplementary file 3
Sequence-based reagent	eMagB^{F} ATGGGACATACC CTCTACGCGCCG GGGGGTTATGAC ATCATGGGTTAC CTCAGACAGATC AGAAACCGGCCG AACCCACAAGTG	This paper	GenBank accession number: MW203025	See Main Text, Materials and Methods and Supplementary file 3

	GAGCTGGGACCC GTCGACCTCTCC TGCGCCCTCGTG CTGTGTGACCTT AAGCAGAAGGAC ACCCCTGTGGTG TACGCCTCCGAA GCATTCCTGGAG ATGACCGGGTAC AACAGACACGAA GTGCTGGGACGG AACTGCCGCTTC CTGCAATCCCCG GATGGAATGGTG AAGCCTAAGTCA ACCCGCAAATAC GTGGACTCCAAC ACTATCTTCACC ATGAAGAAGGCC ATTGACCGCAAT GCTGAGGTGCAA GTGGAAGTGGTG AACTTCAAGAAG AACGGACAGCGC TTCGTCAACTTC CTGACTATGATT CCCGTGCGGGAC GAAACCGGCGAA TACCGGTACAGC ATCGGGTTTCAG TGCGAGACTGAG			
Sequence-based reagent	eMagA ATGGGACACACT CTTTACGCCCCT GGAGGATACGAC ATTATGGGATAT TTGGATCAGATT GCGAACCGCCCA AACCCTCAGGTC GAACTGGGGCCT GTGGACCTGTCA TGTGCCCTGATC CTGTGCGATCTG AAGCAAAAGGAC ACTCCGATCGTC TACGCCTCGGAA GCCTTCTTGGAG ATGACCGGATAC AACAGACATGAG GTGCTCGGCAGG AACTGCAGATTC CTGCAGTCCCCC GACGGGATGGTG AAACCAAAGTCG ACTCGCAAATAT GTGGACTCGAAC ACGATCTACACC ATCAAGAAGGCC ATCGACCGGAAC	This paper	GenBank accession number: MW203026	See Main Text, Materials and Methods and Supplementary file 3

	GCCGAGGTCCAG GTGGAGGTGGTC AACTTTAAGAAG AACGGCCAGCGG TTCGTGAACTTT CTGACCATCATT CCGGTCCGGGAT GAAACCGGAGAG TACAGATACTCC ATCGGATTCCAG TGCGAAACCGAA			
Sequence-based reagent	eMagB ATGGGACATACC CTCTACGCGCCG GGGGGTTATGAC ATCATGGGTTAC CTCAGACAGATC AGAAACCGGCCG AACCCACAAGTG GAGCTGGGACCC GTCGACCTCTCC TGCGCCCTCGTG CTGTGTGACCTT AAGCAGAAGGAC ACCCCTGTGGTG TACGCCTCCGAA GCATTCCTGGAG ATGACCGGGTAC AACAGACACGAA GTGCTGGGACGG AACTGCCGCTTC CTGCAATCCCCG GATGGAATGGTG AAGCCTAAGTCA ACCCGCAAATAC GTGGACTCCAAC ACTATCTACACC ATGAAGAAGGCC ATTGACCGCAAT GCTGAGGTGCAA GTGGAAGTGGTG AACTTCAAGAAG AACGGACAGCGC TTCGTCAACTTC CTGACTATGATT CCCGTGCGGGAC GAAACCGGCGAA TACCGGTACAGC ATCGGGTTTCAG TGCGAGACTGAG	This paper	GenBank accession number: MW203027	See Main Text, Materials and Methods and Supplementary file 3
recombinant DNA reagent	nMagHigh1-EGFP-CAAX	(Kawano et al., 2015) PMID: 25708714	Addgene #67300	

recombinant DNA reagent	pMagFast2(3x)-iRFP	(Kawano et al., 2015) PMID: 25708714	Addgene #67297	
recombinant DNA reagent	iSH2-pMag(3x)-iRFP	(Kawano et al., 2015) PMID: 25708714	Addgene #67298	
recombinant DNA reagent	nMagHigh1-EGFP-Mito	This paper		See Materials and Methods PCR primers: Primer Fw: 5' CGTCAGATC CGCTAGCAT GGGACACAC TCTTTACG Primer Rw: 5' TGCACCTGC ACTCGAGCC CCCTTGTACA GCTCGTC 3
recombinant DNA reagent	pGFP-OMP25	(Nemoto and De Camilli, 1999) PMID: 10357812		
recombinant DNA reagent	pMagFast2(1x)-TagRFP-T	This paper		See Main Text, Materials and Methods and Supplementary file 2 InFusion PCR primers: Primer Fw: 5' GTTTAAACTT AAGCTTgccac catgggaCATAC CCTCTACGC GCCG Primer Rw: 5' AAACGGGCC CTCTAGATCA

				CTTGTACAGC TCGTCC
recombinant DNA reagent	pMagFast2(3x) - TagRFP-T	(Benedetti et al., 2018) PMID: 2946375 0		
recombinant DNA reagent	eMagA^{F}- EGFP-Mito	This paper	Addgene #162243	See Main Text, Materials and Methods and Supplementary file 1
recombinant DNA reagent	eMagA- EGFP-Mito	This paper	Addgene #162244	See Main Text, Materials and Methods and Supplementary file 1
recombinant DNA reagent	eMagB- TagRFP-T	This paper	Addgene #162252	See Main Text, Materials and Methods and Supplementary file 2
recombinant DNA reagent	eMagB^{F}- TagRFP-T	This paper	Addgene #162253	See Main Text, Materials and Methods and Supplementary file 2
recombinant DNA reagent	ER-EGFP- eMagA	This paper	Addgene #162245	See Main Text, Materials and Methods and Supplementary file 1
recombinant DNA reagent	ER- mCherry- eMagA	This paper	Addgene #162248	See Main Text, Materials and Methods and Supplementary file 1
recombinant DNA reagent	eMagA- mCherry- Mito	This paper	Addgene #162251	See Main Text, Materials and Methods and Supplementary file 1

recombinant DNA reagent	eMagB-iRFP-Mito	This paper	Addgene #162250	See Main Text, Materials and Methods and Supplementary file 1
recombinant DNA reagent	Lys-eMagB-iRFP	This paper	Addgene #162249	See Main Text, Materials and Methods and Supplementary file 1
recombinant DNA reagent	TagRFP-T-VAPB$_{(1-218)}$-eMagB	This paper	Addgene #162255	See Main Text, Materials and Methods and Supplementary file 2
recombinant DNA reagent	Lys-eMagA-EGFP	This paper	Addgene #162246	See Main Text, Materials and Methods and Supplementary file 1
recombinant DNA reagent	Lys-nMagHigh1-EGFP	(Benedetti et al., 2018) PMID: 29463750		
recombinant DNA reagent	Lamp1-iRFP	This paper		See Materials and Methods. InFusion PCR primers: Primer Fw: 5' CTCAAGCTTCGAATTCATGGCGGCCCCCGGCAGC Primer Rw: 5' GGCGACCGGTGGATCCGGGATAGTCTGGTAGCCTGC
recombinant DNA reagent	piRFP670-N1	(Shcherbakova DM and Verkhusha VV,2013) PMID: 237707	Addgene #45457	

		55		
recombinant DNA reagent	eMagA^{F}-EGFP-PM	This paper	Addgene #162247	See Main Text, Materials and Methods and Supplementary file 1
recombinant DNA reagent	mCherry-eMagB^{F} - 5ptase$_{OCRL}$	This paper	Addgene #162254	See Main Text, Materials and Methods and Supplementary file 2 InFusion PCR primers: Primer Fw: 5' TCTCGAAGCG CGGCCGCGAT GGGACATACC CTCTACGCG Primer Rw: 5' GAATGTTGAC ATACGATCGG GTACCTCCGC TGCCTCC
recombinant DNA reagent	mCherry-pMagFast2(3x)-5ptase$_{OCRL}$	(Benedetti et al., 2018) PMID: 29463750		
recombinant DNA reagent	iRFP-PH$_{PLC\delta}$	(Idevall-Hagren et al., 2012) PMID: 22847441		
recombinant DNA reagent	TagRFP-T-eMagB-PH$_{OSBP}$	This paper		See Main Text, Materials and Methods and Supplementary file 2 InFusion PCR primers:

				Primer Fw: 5' CACCTGCATG CGGCCGCGCC ACCATGGTGT CTAAGGG Primer Rw: 5' CGGGACCTCG AGGTTAACTC ATTTCTGCCTT GATCTGTAGTA G
recombinant DNA reagent	GFP-PH_{OSBP}	Dr. Tim Levine, UCL Institute of Ophthalmology		
recombinant DNA reagent	iRFP-P4C	This paper		See Materials and Methods InFusion PCR primers: Primer Fw: 5' CGCTAGCGCT ACCGGTATGG CGCGTAAGGT CGATCTCACC Primer Rw: 5' AGTCCGGACT TGTACAtGCGT TGGTGGTGGG CGGC
recombinant DNA reagent	GFP-$P4C_{SidC}$	Dr. Yuxin Mao, Cornell		
commercial assay or kit	In-Fusion HD Cloning Kit	Takara Bio	Cat. No. 638910	
cell line (*Homo-sapiens*)	HeLa	ATCC	CCL-2^{TM}	

cell line (*Cercopithecus aethiops*)	COS-7	ATCC	CRL-1651™	
cell line (*Homo-sapiens*)	HeLa VAPDKO	(Dong et al., 2016)		Cell line generated in the De Camilli Lab
biological sample (*Mus musculus*)	Primary hippocampal neurons	Charles River	C57BL/6	
chemical compound, drug	Itraconazole	Tocris	Cat. No. 5981	
Software, algorithm	TBLASTN	NCBI	(TBLASTN, RRID:SCR_011822)	
software, algorithm	PyMOL	Schrödinger, Inc.	(PyMOL, RRID:SCR_000305)	PyMOL 2.3.5.
software, algorithm	Fiji	NIH	Fiji, RRID:SCR_002285	ImageJ Version: 2.0.0-rc-69/1.52p, Wayne Rasband, National Institute of Health, USA, http://fiji.sc/wiki/index.php/Fiji
software, algorithm	MATLAB	MathWorks	(MATLAB, RRID:SCR_001622)	MATLAB 2019a

software, algorithm	Graph Pad	Graph Pad Software	(GraphPad Prism, RRID:SCR_002798)	GraphPad Prism 8.2.1